Estimates of spectral wave attenuation in Antarctic sea ice, using model/data inversion

W. Erick Rogers[1,1], Michael Meylan[2,2], and Alison Kohout[3,3]

[1]Naval Research Laboratory
[2]University of Newcastle
[3]National Institute of Water and Atmospheric Research

November 30, 2022

Abstract

A model-data inversion is applied to an extensive observational dataset collected in the Southern Ocean north of the Ross Sea during late autumn to early winter, producing estimates of the frequency-dependent rate of dissipation by sea ice. The modeling platform is WAVEWATCH III® which accounts for non-stationarity, advection, wave generation, and other relevant processes. The resulting 9477 dissipation profiles are co-located with other variables such as ice thickness to quantify correlations which might be exploited in later studies to improve predictions. An average of dissipation profiles from cases of thinner ice near the ice edge is fitted to a simple binomial. The binomial shows remarkable qualitative similarity to prior observation-based estimates of dissipation, and the power dependence is consistent with at least three theoretical models, one of which assumes that dissipation is dominated by turbulence generated by shear at the ice-water interface. Estimated dissipation is lower closer to the ice edge, where ice is thinner, and waveheight is larger. The quantified correlation with ice thickness may be exploited to develop new parametric predictions of dissipation.

1

Estimates of spectral wave attenuation in Antarctic sea ice, using model/data inversion

W. Erick Rogers, Naval Research Laboratory, Stennis Space Center, MS, U.S.A.

Michael H. Meylan, The University of Newcastle, Australia

Alison L. Kohout, National Institute of Water and Atmospheric Research (NIWA), New Zealand

Corresponding author: W. Erick Rogers (erick.rogers@nrlssc.navy.mil)

Keywords

Ocean waves; sea ice; spectral wave model; wave-ice interaction; WAVEWATCH III; dissipation by sea ice

Highlights

- Frequency dependence of dissipation by sea ice is estimated for an extensive dataset.

- Power dependence on frequency is found to be power two to four.

- A negative correlation is found between waveheight and dissipation rate.

- A positive correlation is found between ice thickness and dissipation rate.

- Correlation of dissipation with ice thickness can be exploited in predictive models.

Long-form highlights

- Frequency dependence of dissipation by sea ice is estimated for an extensive dataset (9477 records) near Antarctica using model/data inversion.

- Power dependence of dissipation rate on frequency in thinner ice near the ice edge is found to be well represented by a power two and four binomial, or power 3.5 monomial.

- Estimated dissipation is lower closer to the ice edge, where ice is thinner, and waveheight is larger.

- The positive correlation between ice thickness and dissipation rate can potentially be exploited for predictive models.

Abstract

A model-data inversion is applied to an extensive observational dataset collected in the Southern Ocean north of the Ross Sea during late autumn to early winter, producing estimates of the frequency-dependent rate of dissipation by sea ice. The modeling platform is WAVEWATCH III® which accounts for non-stationarity, advection, wave generation, and other relevant processes. The resulting 9477 dissipation profiles are co-located with other variables such as ice thickness to quantify correlations which might be exploited in later studies to improve predictions. An average of dissipation profiles from cases of thinner ice near the ice edge is fitted to a simple binomial. The binomial shows remarkable qualitative similarity to prior observation-based estimates of dissipation, and the power dependence is consistent with at least three theoretical models, one of which assumes that dissipation is dominated by turbulence generated by shear at the ice-water interface. Estimated dissipation is lower closer to the ice edge, where ice is thinner, and waveheight is larger. The quantified correlation with ice thickness may be exploited to develop new parametric predictions of dissipation.

1. Introduction

During the past 20 years, open-ocean spectral wave modeling has achieved high levels of accuracy, e.g. Bidlot (2018), primarily driven by improvements to accuracy in wind forcing and physics parameterizations (e.g. Ardhuin et al. 2010, Liu et al. 2019). However, areas near coastlines and the sea ice margins remain a challenge, with relatively large errors and therefore substantial improvements possible (e.g. Cavaleri et al. 2018 and Sutherland et al. 2018, respectively). Predictions near the ice edge fall into two broad categories: the off-ice wind scenario, and the on-ice wave scenario. In the former case, errors are caused by uncertainty in the ice edge location, and challenges with describing the rarely-studied conditions of growth in partial ice cover and the ubiquitous atmospheric instability (i.e. cold air blowing from the ice onto warmer water; see Gemmrich et al. (2018)). Modeling the on-ice wave scenario *also* suffers from the uncertainty of the ice edge position. In addition, wave conditions within the ice are dominantly determined by the model's representation of dissipation by sea ice. Fundamentally, this dissipation is strongly dependent on frequency (e.g. Wadhams et al. 1988). The objective of this paper is to use observational data to estimate this frequency-dependent dissipation rate and study possible dependencies, to guide future improvements to parameterizations of dissipation used by spectral wave models, and thence improvements to the accuracy of these models in on-ice wave conditions.

More recently, there has been a surge in research activity on the topic of wave-ice interaction. This includes theoretical studies, numerical modeling studies, laboratory studies, and studies using field observations, either in situ observations or those from remote sensing. To demonstrate this quantitatively, we surveyed peer-reviewed articles published from 2015 to 2019. We found 32 articles for which the dissipation of wave energy by sea ice is a primary feature (e.g. Toffoli et al. 2015, Ardhuin et al. 2016, Asplin et al. 2018, Boutin et al. 2018, Herman et al. 2019, Marchenko et al. 2019, Voermans et al. 2019, Yue et al. 2019). In addition, we find nine other articles which are primarily concerned with both dissipation and changes to wavelength caused by the ice (e.g. Li et al. 2015a, Zhao et al. 2017), and four that are primarily concerned with the changes to wavelength (e.g. Sree et al. 2018). We find nine other articles primarily about the scattering and reflection of wave energy by sea ice (e.g. Montiel et al. 2016, Orzech et al. 2016, Bennetts and Williams 2015). We find 15 articles which treat the impact of

waves on ice, either by fracturing the ice (e.g. Bennetts et al. 2017) or by determining the ice type during growth (Roach et al. 2018, Shi et al. 2019). We find six review articles during this period (e.g. Shen 2019). A detailed review of all these topics is beyond the scope of this paper, but the latter review article and Squire (2020) are a good starting point for interested readers.

Among wave-ice interaction studies, observational campaigns in the southern hemisphere are in the minority. To the authors' knowledge, the earliest study was that of Robin (1963) describing measurements using a ship-borne wave recorder in the Weddell Sea during 1959-1960. These measurements used early technology, and since wave observations were local to the ship, results were described not in terms of dissipation rate (the critical parameter required by a modern numerical wave model), but instead in terms of the distance of penetration of swells into the ice field. Robin found that this value depends on three rather intuitive parameters: wave period (or length), ice thickness, and floe size, with the first being important in all cases, the second being important for long waves, and the third being important for shorter waves. Doble and Wadhams (2006) and Doble (2009) describe a buoy deployment in the Weddell Sea in 2000, with particular attention to autumn ice growth and interaction with pancake and frazil ice. Doble and Bidlot (2013) study data from a buoy from the same deployment, but five months later (late winter/early spring), when the buoy was in pack ice during an energetic breakup event. Kohout et al. (2014) and Meylan et al. (2014) analyzed data from a buoy deployment during the SIPEX II voyage in 2012 north of Wilkes Land, Antarctica; these data have since been used also by Li et al. (2015b) and Liu et al. (2020). In July 2017, C. Eayrs (New York Univ.) and others deployed wave-buoys north of Queen Maud Land, Antarctica (Vichi et al. 2019); Alberello et al. (2019) study pancake and frazil ice formation during the same experiment.

The present study uses another buoy dataset collected only a month earlier (June 2017), part of a larger dataset obtained north of the Ross Sea. This builds on a previous analysis by Kohout et al. (2020), who looked at the decay rate of total energy (i.e. significant waveheight) within the sea ice for the full wave buoy dataset (April to July 2017). That study found that the decay is generally linear exponential, and concluded that dissipation increases with ice concentration. The present study uses model-data inversion to estimate the frequency distribution of the dissipation rate. A notable advantage of the model-data inversion method is that it does not require that wave energy travels primarily along an axis between two buoys.

A remarkable feature of the Kohout et al. (2020) dataset is its size: we are not aware of any prior study of spectral dissipation by sea ice using a larger dataset. The full dataset includes over 14,000 spectra (21 April to 26 July), and the present study uses 9477 of those records for co-locations during 6 to 30 June. This large population enables a robust evaluation of the correlation between the dissipation rate and several additional variables ("tertiary variables"), such as satellite-based ice thickness estimates.

The paper is structured as follows. Section 2 reviews the literature on the topic of the frequency dependence of dissipation. Section 3 gives a brief overview of the field experiment. Section 4 describes the wave model, Section 5 describes the model-data inversion, and Section 6 presents the results of the analysis. Section 7 presents possible simple fits to the mean dissipation profiles. Summary and conclusions are given in Section 8.

2. Brief review of frequency dependence in the literature

Modern numerical wave models, e.g. WAVEWATCH III®, introduced in Section 4.1, compute the dissipation by sea ice as $S_{ice} = -2C_g k_i E$, where C_g is the group velocity, E is spectral energy density, and k_i is the exponential rate of spatial decay of wave amplitude or waveheight, e.g. $a(x) = a_0 e^{-k_i x}$, where a is the amplitude, a_0 is the initial amplitude and x is the distance. Observations suggest that the S_{ice} source term is a low-pass filter. Contrary observations of a "roll-over" effect, i.e. lower dissipation rate at high frequencies relative to mid-frequencies, are suspected as an artifact of disregarding local windsea growth (Wadhams et al. 1988; Rogers et al. 2016; Li et al. 2017) or of failing to account for instrument noise (Thomson et al. 2020). Parametric representation of the low-pass filter is determined by the shape of $k_i(f)$, where f denotes frequency. If the $k_i(f)$ profile increases continuously $k_i(f) \propto f^n$ may be suitable, and is in fact widespread in the literature. Here, we summarize values of power dependence n which we have found in the literature.

- ❏ Fit to data derived from sonar observations in Greenland Sea, Wadhams (1978), according to Squire 1998, n=2.
- ❏ A viscoelastic model, the first of two new models proposed by Meylan et al. (2018), n=2.
- ❏ A viscoelastic model, the second of two new models proposed by Meylan et al. (2018), n=3.
- ❏ Derived from buoy observations near Antarctica, Meylan et al. (2014), binomial with n=2 and 4. Meylan et al. (2018) report a best fit of n=1.9 for the same dataset.
- ❏ Derived from buoy observations in pancake ice near Antarctica, Doble et al. (2015): n=2.1. Meylan et al. (2018) report a best fit of n=2.9 for the same dataset. Sutherland et al. (2019) report a best fit of n=3.8 for this dataset, using a subset of the total frequency range.
- ❏ Derived from observations in the Greenland and Bering Seas, reported in the seminal work of Wadhams et al. (1988). This dataset is highly scattered, either due to highly varied conditions, or less precise methods. In Meylan et al. (2018), a best fit of n=3.6 is reported for this dataset.
- ❏ Derived from buoy observations in and near the Beaufort Sea, Rogers et al. (2016, 2018a), binomial with n=2 for the first term and n=4 to 5 for the second.
- ❏ For the same experiment in the Beaufort Sea, Cheng et al. (2017) estimated dissipation rates, and Meylan et al. (2018) report a best fit of n=3.6.
- ❏ Viscoelastic model of Robinson and Palmer (1990) as reduced by Meylan et al. (2018), n=3. See also Liu et al. (2020).
- ❏ Boundary layer model, by F. Ardhuin (newer variant of 'IC2' in WAVEWATCH III): turbulent regime: n=3 and laminar regime: n=3.5. This is described in Appendix B of Stopa et al. (2016).
- ❏ Inextensible surface cover, Weber (1987) (from Lamb 1932): n=3.5. Weber (1987) invokes the concept of eddy viscosity to represent turbulence in the lower/water layer, such as might occur due to shear at the ice/water interface.
- ❏ Empirical fit to airborne data by Sutherland et al. (2018): n=3.5.
- ❏ Friction model, Kohout et al. (2011): n=4.
- ❏ Viscous water model, Lamb (1932), Weber (1987): n=5.
- ❏ Empirical fit to laboratory data by Rabault et al. (2019): n=6 to 6.5.

❏ Viscous ice model, Keller (1998) (this can be recovered in WAVEWATCH III using the 'IC3' viscoelastic model with zero elasticity): n=7.
❏ A viscoelastic model introduced in Mosig et al. (2015) and implemented in WAVEWATCH III by Liu et al. (2020). It is referred to as the "extended Fox and Squire" (EFS) model in the latter paper. Meylan et al. (2018) call it the "viscous Greenhill" model, and find: n=11.

More detailed descriptions of some of these can be found in Meylan et al. (2018) and Rogers et al. (2018a,b).

3. Field experiment (overview)

The wave observations used in this study are described in Kohout and Williams (2019) and Kohout et al. (2020). Here, we provide a brief overview.

During the Polynyas, Ice Production, and seasonal Evolution in the Ross Sea (PIPERS) expedition in 2017, 14 waves-in-ice observation systems (WIIOS, Kohout et al. 2015) were deployed on Antarctic sea ice, in the Southern Ocean north of the Ross Sea. Four buoys were deployed during the transit south toward the Ross Sea on 21-22 April 2017, and ten more were deployed during the outbound transit, 30 May to 3 June, with the first data recorded on 2 June. The inbound deployment was near 172˚E, and the outbound deployment was approximately 470 km east of that, near 184˚E. Buoy survival durations varied significantly, with the last record of the western (inbound) group coming on 6 July (10.8-week duration) and the last record of the eastern (outbound) group on 26 July (7.7-week duration). Figure 1 shows the geographic location of the PIPERS deployment relative to three other notable wave-ice field experiments near Antarctica: an experiment in 2000 in the Weddell sea reported by Doble and Wadhams (2006); an experiment in 2012 north of Wilkes Land reported in Kohout et al. (2014) and Meylan et al. (2014); and an experiment in July 2017 with data collected by C. Eayrs, north of Queen Maud Land, reported in Vichi et al. (2019).

One buoy in the eastern group had a GPS failure, so effectively there are four and nine buoys in the west and east group, respectively. The spectral energy, $E(f)$, data are provided with a precision of 1×10^{-6} m^2/Hz. The full dataset includes 23,206 spectra with valid GPS coordinates. Of these, records with significant waveheight H_{m0}<0.1 m are omitted here to improve the overall signal-to-noise ratio, leaving 14,602 spectra. In this study, we analyze data from the eastern (outbound) grouping during 24 days of the transition from late autumn to early winter: 6 to 30 June. This subset includes 9511 spectra and all of the large wave events (observed H_{m0}>3 m) of the full dataset. As will be described in Section 5, the model-data inversion requires us to omit cases of low ice concentration, leaving 9477 spectra. The final number represents 41% of the full dataset and is at least 35 times larger than the dataset collected in SIPEX II (with 268 records), as previously noted by Kohout and Williams (2019).

Six of the buoys in the eastern group have more than 500 records each; information about these buoys are described in Table 1, and time series of the distance to the ice edge[1] for each of these six buoys are shown in Figure 2. Each wave buoy is deployed directly on the ice, either on an

---

[1] see Section 6.1 for definition

existing floe or on continuous ice. The buoys are designed never to be retrieved, so all processing is performed onboard and data is sent by satellite telemetry. The primary component of the buoy is an Inertial Measurement Unit (IMU). Two of the nine buoys in the eastern grouping deployed deepest in the ice used high precision IMUs, with the expectation that they would experience the lowest wave energy; these included buoy 14, listed in Table 1. The buoys were thoroughly tested prior to PIPERS (Kohout and Williams 2019).

The WIIOS buoys record the motion of the floe upon which they rest. They can be expected to measure the motion of the underlying sea surface if either the floe is small relative to the wavelength being measured, or if the floe is large but bending freely such that it follows the sea surface. In either case, the response function is 1:1. However, if the floe is large and rigid, there will be an unknown deviation, particularly for higher frequencies.

In this region and season, southerly katabatic winds push new ice northward from the Ross Sea (Kohout and Williams 2019) while wave conditions are dominated by extratropical storms in the Southern Ocean which generate swells arriving primarily from the northwest. The waves may transfer momentum to the mean flow and ice as they decay (Liu and Mollo-Christensen 1988; Stopa et al. 2018), which would result in a southward stress countering the northward wind stress. The eastern buoys were deployed along a south to north (meridional) transect, but they drifted to a roughly west-southwest to east-northeast orientation by mid-June. (Diagrams and an animation of the buoy tracks are provided with the Supplemental Information.) Ship-based ice observations were made using the Antarctic Sea Ice Processes and Climate (ASPeCt) protocol (Worby 1999). Ice consisted primarily of floes from new sheet ice (15-30 cm thick) and first-year ice (30 to 70 cm thick). This is summarized in Table 1, and more details can be found in Kohout et al. (2020).

Figure 3 shows an example of wave spectra for the six buoys, using the same color scheme as used in Figure 2. By comparing the two figures, one can see the correspondence between the damping of the spectrum and distance from the ice edge, with damping occurring first at higher frequencies, and then more noticeably at the dominant frequencies for the buoys farther in the ice. At the lowest energy levels, the high-frequency tail slope is flatter than what might be expected in a spectrum in ice, recalling that ice acts as a low-pass filter, which should result in a steep slope. The tail may be "propped up" by an unknown physical process, or by instrument noise. The energy levels below which the spectral tails are noticeably elevated—either by noise or the unknown physical process—are indicated in Figure 3. This is discussed further in Section 6.3 and the Appendix.

Table 1. WIIOS deployments for PIPERS-17: Only buoys in eastern grouping with 500 or more data records are included. Notation: h_{ice}, d_{ice}, a_{ice} are ice thickness, floe size, and concentration respectively. Buoys are given here in order of deployment, from south to north. Note that the sizes of the floes on which the buoys are deployed are not known generally. Floes may have broken after deployment, and some buoys far from the ice edge were actually deployed on the continuous ice and became "buoys on floes" later.

Buoy #	Buoy ID	floe upon which the buoy is deployed		most prevalent ice near the buoy, from nearest ASPeCt record			# of spectra	init. dist. from ice edge (km)
		h_{ice} (cm)	d_{ice} (m)	a_{ice}	h_{ice} (cm)	d_{ice} (m)		
14	A-34*	54	N/A (cont. ice)	100%	50	100-500	509	244
5	B-25	60	100	100%	60, 75	20-100	1349	175
6	B-26	70	20	100%	30	20-100	1746	153
7	B-27	36	40	50%	30	20-100	1830	151
9	B-29	50	40	100%	20	<20 (cake)	1668	133
10	B-30	75	20	100%	30	20-100	2052	118

* equipped with high-precision "Kistler" accelerometer

0 and 300 m depth contours
red: Doble-00 ; green=SIPEX-12
blue=PIPERS-17 ; purple=Eayrs-17
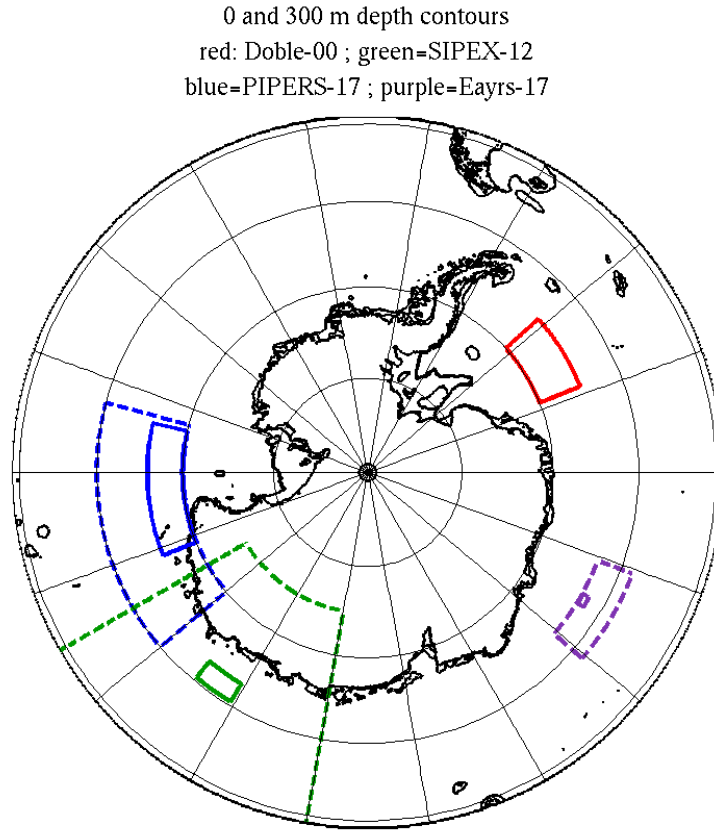
Figure 1. The geographic location of the observational campaign used in this paper (PIPERS-17) is marked in blue. Other observational studies are indicated as historical context and potential further work with comparable inversion exercises. Dashed colored lines are model grids and solid colored lines approximately denote the bounds of observational data for each case. Dashed blue box (for PIPERS-17) is the model domain of this study. Dashed green box (for SIPEX-12) is from Li et al. (2015b) (1/4° resolution). Dashed purple box (for Eayrs-17) pertains to a hindcast that will be reported on separately.
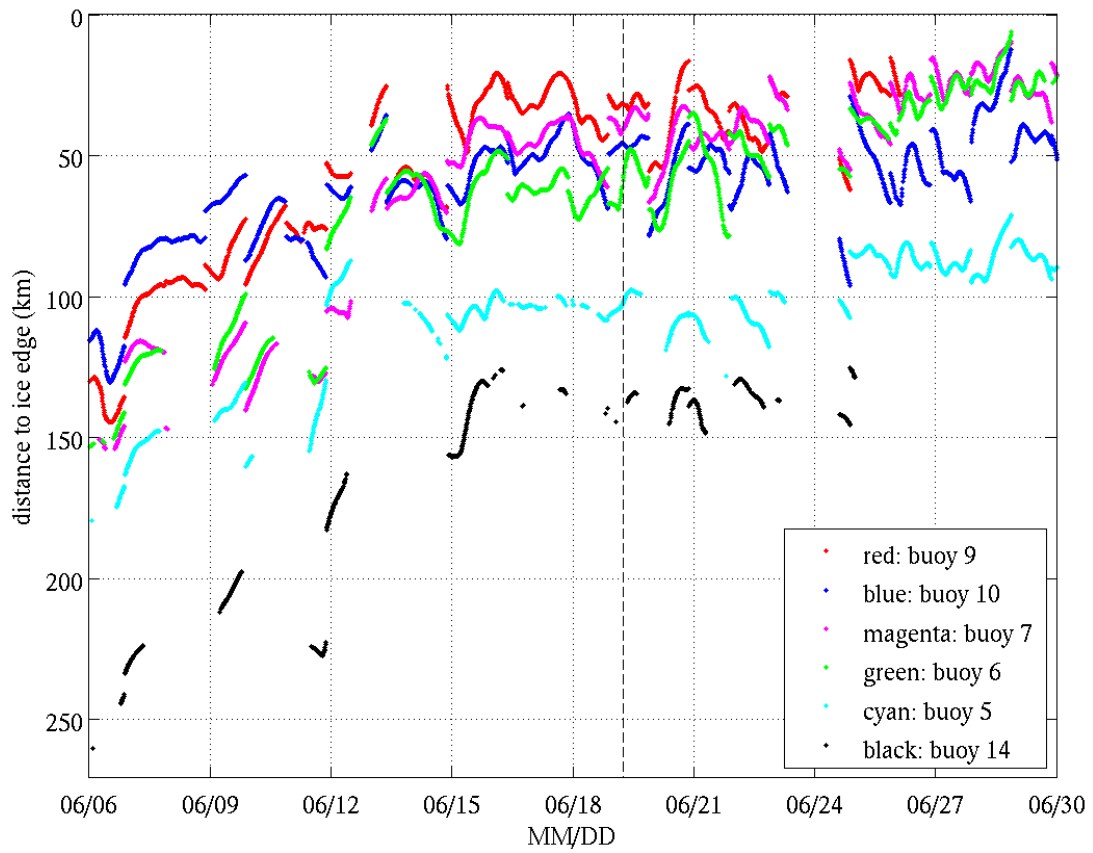
Figure 2. Positions of the six buoys, relative to the ice edge. The vertical line here indicates the time used in Figures 3, 4, and 5.
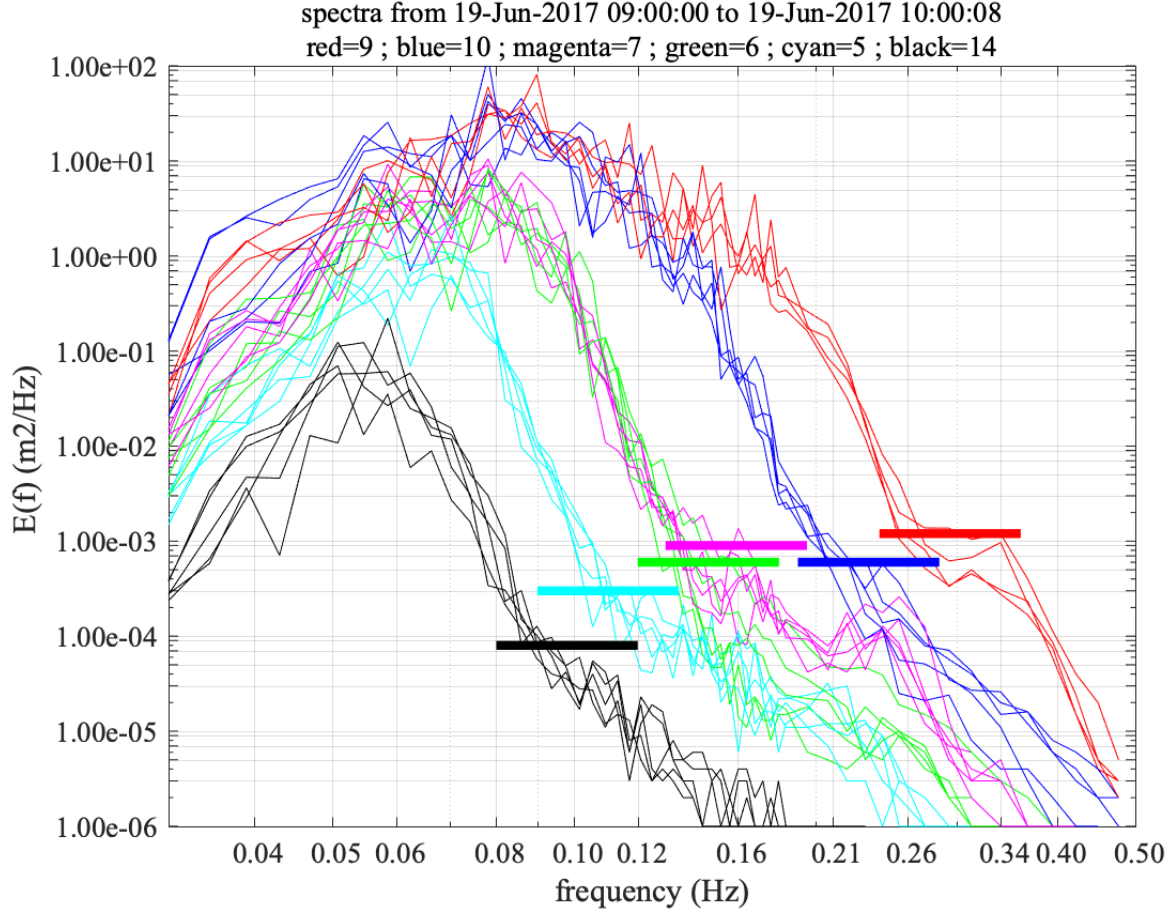
Figure 3. Energy spectra from the six buoys during the period of 0900 to 1000 UTC 19 June 2017. This uses the same color scheme as Figure 2. The thick horizontal lines indicate energy levels below which the tail is visibly "propped up", presumably by instrument noise.

4. Wave model

4.1. General description

The wave model used in this study WAVEWATCH III® (WW3, Tolman 1991, WW3DG 2016). This is a phase-averaged spectral model for which the prognostic variable is wave action spectral density, which is the wave energy spectral density divided by the angular wave frequency: $N = E/\sigma$, where $\sigma = 2\pi f = 2\pi/T$ (T denoting wave period). The spectrum is a function of wavenumber or angular frequency (k or σ), direction (θ), space (x, y or longitude, latitude), and time (t). The left-hand side of the radiative transfer equation includes terms for the time rate of change and propagation in the four dimensions (kinematics), while the right-hand side provides source functions (dynamics):

$$\frac{\partial N}{\partial t} + \nabla \cdot \vec{c} N = \frac{S}{\sigma} \tag{1}$$

where $\vec{c}$ is a four-component vector describing the propagation velocities in x, y, k, and θ. For example, in the absence of currents, c_x is the x-component of group velocity C_g. The sum of all source functions is denoted as S, and individual source functions are indicated with an appropriate subscript: S_{in}, S_{wc}, S_{nl4}, and S_{ice} being energy input from wind, dissipation by whitecapping, four-wave nonlinear interactions, and dissipation by sea ice, respectively. We use the "source term package" of Ardhuin et al. (2010) known as 'ST4', for S_{in} and S_{wc}. In this package, swell dissipation (weak losses of energy not associated with breaking) is formally part of S_{in}. For S_{nl4}, we use the Discrete Interaction Approximation (DIA) of Hasselmann et al. (1985).

S_{ice} is scaled by areal ice fraction a_{ice}, following Doble and Bidlot (2013), and the default behavior of WW3 (WW3DG 2016) is to scale open water source terms by the open water fraction, $1 - a_{ice}$:

$$S = (1 - a_{ice})(S_{in} + S_{wc} + S_{nl4}) + a_{ice}S_{ice} \qquad (2)$$

The scaling of open water source terms is an essential concept in our analysis. In case of full omission of the scaling for all three terms, we have:

$$S = S_{in} + S_{wc} + S_{nl4} + a_{ice}S_{ice} \qquad (3)$$

The scaling of S_{in} is particularly debatable, since the transfer of energy from wind to waves occurs through normal stresses, and one can easily imagine that normal stresses remain effective (or partially effective) in cases where the ice is composed of frazil, brash, or pancakes, or when floe size is small relative to wavelength. The optimal representation is somewhere between (2) and (3) and is probably frequency-dependent. The scaling of S_{nl4} is similarly in doubt: see discussion of relevant literature in Rogers et al. (2016). Scaling of S_{wc}, on the other hand, is unlikely to be as consequential, since in ice, S_{wc} will tend to be small or zero.

Where k_i gives the exponential decay rate of amplitude in the space domain, the exponential decay of energy in the time domain, prior to scaling by a_{ice}, is computed as $D_{ice} \equiv S_{ice}/E = -2C_g k_i$. The group velocity C_g can, in principle, be affected by ice cover, particularly in frequencies above 0.3 Hz (Cheng et al. 2017; Collins et al. 2018), but here we simply assume that the group velocity is the open water group velocity.

In the analysis of observational studies, where a positive correlation between dissipation rate and ice concentration is reported, it is crucial to note whether the authors are referring to S_{ice} or $a_{ice}S_{ice}$. In the case of Kohout et al. (2020), the positive correlation is referring to the latter, scaled term. In Section 6.3, we look at the correlation between ice concentration and the former, unscaled term (or, more precisely, k_i).

4.2. Implementation for this study

The specific implementation of WW3 used in this study is described in this section.

Wind forcing in the form of 10-m wind vectors comes from archives of the U.S. Navy's global atmospheric model, NAVGEM (Hogan et al. 2014), at 3-hourly intervals and 1/4˚ geographic resolution. Ice concentration forcing for the nested grid come from AMSR2 analyses using the

"ARTIST" algorithm, Spreen et al. (2008) and Beitsch et al. (2013, 2014). This ice concentration product is at relatively high geographic resolution (median spacing is 3.05 km) but relatively low temporal resolution (one field every 24 hours).

The wave model grid receives boundary forcing from a global model hindcast. The global model was run from 0000 UTC 23 May 2017 to 0000 UTC 30 June 2017. The global grid design known as "Irregular-Regular-Irregular" (Rogers and Linzell 2018) is used. Resolution is 1/4° at low latitudes and 18 km south of 50°S.

The 'ST4' package for open water source terms is used with the 'DIA' method of computing nonlinear interactions. The spectral grid includes 36 directional bins and 31 frequency bins (0.0418 to 0.73 Hz, logarithmically spaced). The wind input source term of Ardhuin et al. (2010) requires specification of a wind input calibration parameter, β_{max}; a value of 1.2 is used for these hindcasts.

The nested grid bounds are indicated in Figure 1 and Figure 4. The PIPERS grid is bounded by 140°E, 195°E, 70.1°S, and 60°S and contains 292×10^3 sea points. The computational grids are polar stereographic and match the grids of the ice concentration input (3.05 km median resolution).

The northern limit of the nest, 60°S, is selected so that all relevant ice is entirely inside the nest during the simulation period. This implies that the S_{ice} settings of the global model are inconsequential to the inversion.

The WW3 nest and example output are shown in Figure 4. The time period, 0900 UTC 19 June 2017, corresponds to the time period used in Figure 3. Buoy positions are marked with filled circles, using the color scheme of Figure 3. Buoy 9 (red circle) and 10 (blue circle) are used later, in Figure 5. Note that for this case, the mean wave direction approximately matches the axis between these two buoys. An animation of images similar to Figure 4 are provided with the Supplemental Information.
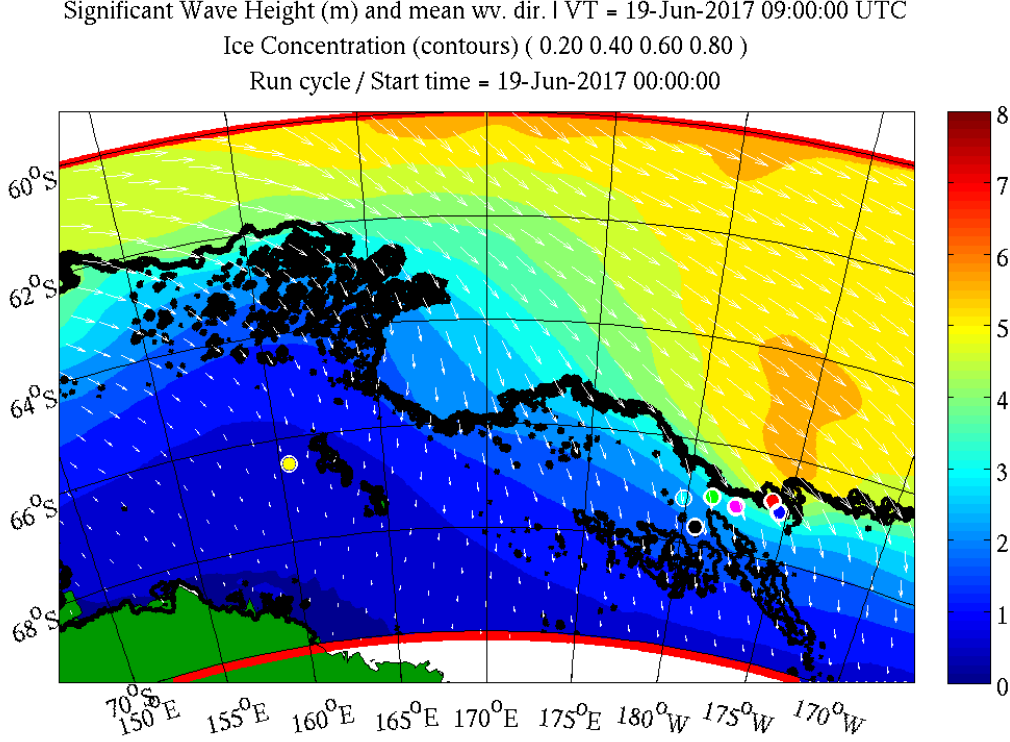
Figure 4. Wave conditions predicted by WW3 for the period of 0900 UTC 19 June 2017. Red lines indicate the northern and southern boundary of the WW3 nest. Colors indicate the significant waveheight in meters. Arrows indicate the mean wave direction. Contours indicate ice concentration at 20%, 40%, 60%, and 80%. This is the same time period used in Figure 3. Buoys are marked with dots, using the color scheme of the prior two figures. The yellow dot is the last surviving buoy in the western/inbound buoy group, not used in this paper.

5. Inversion process: introduction

Here we use the inversion method introduced in Rogers et al. (2016). In briefest terms, the objective is to determine the value of attenuation rate $k_i(f)$ which provides a match between the modeled energy density spectrum $E(f)$ and the corresponding observed $E(f)$. Thus, for each observational $E(f)$, a dissipation profile $k_i(f)$ is determined.

The discrete frequencies on which the modeled and observed $E(f)$ are natively described have dissimilar minimum, maximum, and spacing. For the purpose of the inversion, these are remapped to new distributions over the region in which they overlap, 0.042 to 0.472 Hz. These new frequency bins are coarser than either of the native frequency distributions, to increase degrees of freedom and improve stability (e.g. Elgar 1987).

There are 16 coarse frequency bins, with spacing at or near 0.020 Hz at lower frequencies, and spacing at or near 0.039 Hz at higher frequencies. The left (i.e. low frequency) side of the first bin is 0.042 Hz, and the right side of the last bin is 0.472 Hz.

The primary computational component of the inversion consists of repeated simulations with a fixed value of k_i. Linear interpolation is performed between these values to find the "optimal"

14

k_i, where observed $E(f)$ should match the modeled $E(f)$. The process is described and illustrated in Rogers et al. (2016). The inversion here includes 20 k_i values (so 20 hindcasts). The spacing is finer for the smaller values. In units of 1/m, k_i values are: [0, 1e-6, 2e-6 ,..., 2000e-6 , 4000e-6 , 9000e-6]. Note that since negative values of k_i are not included in this set, solutions of negative k_i are effectively disallowed. This is discussed further below.

Since the inversion seeks to match the buoy observations by selecting the optimal k_i value, and the source term S_{ice} is scaled by ice concentration a_{ice}, it does not return a valid solution in cases of a_{ice}=0, and for cases of small a_{ice}, the solution k_i is less stable. Therefore, these cases are omitted. We use the semi-arbitrary cut-off of a_{ice}=0.22. As noted in Section 3, we use data from the eastern buoy group collected during the period starting 0000 UTC 6 June and ending 0000 UTC 30 June 2017.

Attenuation rates are traditionally estimated by computing differences in wave energy measured by two buoys, preferably two buoys along the primary axis of wave propagation, e.g. Meylan et al. (2014). We refer to this herein as the "geometric" method. The model/data inversion method is particularly appropriate here because it does not require that buoy configuration is aligned with the mean wave direction: in this field study, buoys became misaligned over time due to drift (Section 3). Other advantages and disadvantages of the inverse method used here, relative to the geometric method, are summarized in Rogers et al. (2020).

Figure 5 compares the <u>inverse method</u> with the <u>geometric method</u> for a single time period. Colored lines are from the same PIPERS example used in prior figures (0600 to 1200 UTC 19 June 2017). Thin green lines are $k_i(f)$ profiles estimated by the inverse method at the inner buoy, which is #10 in this case. Thin red lines are $k_i(f)$ profiles estimated by the inversion method at the outer (near the ice edge) buoy, which is #9 in this case. There are multiple lines for each because the entire period from 0600 to 1200 UTC 19 June 2017 is used. The inversion estimates $k_i(f)$ at each buoy, independent of other buoys. The thick blue line is the estimate of $k_i(f)$ using the traditional geometric approach and corresponds to an average for the six-hour period. Three reference profiles are also shown in this figure. "SIPEX-12" is the fitted profile from Meylan et al. (2014). "SWIFT WA3" is the profile fitted to an inversion (Rogers et al. 2018b) using SWIFT buoys (Thomson 2012) in "Wave Array 3" of the Sea State field experiment (Thomson et al. 2018). The PIPERS reference profile is an average profile from the present study, denoted "mean 2" (M2), presented in Section 7 and Figure 8.

In the inversion, there is no guarantee that the dissipation of wave energy by sea ice will be much larger than the errors in the wave model. In our case, this was most evident at the two lowest frequency bins (0.042 to 0.08 Hz, i.e. wave periods larger than 12.5 seconds). At low frequencies, k_i is small, and its impact may be lower than model errors, such as the error in the boundary forcing. For example, if our global model is providing boundary spectra that is too weak (low energy), the inversion will seek to compensate by reducing k_i. In our evaluation of profiles, we treat these first two bins with enhanced suspicion.

At high frequencies, another challenge exists. The lower the energy density $E(f)$, the more likely it is to be substantially affected by noise (Figure 3 and Thomson et al. (2020)). We flag $k_i(f)$ solutions as unusable when $E(f) < JE_n$, where E_n is the estimated noise level and J is a subjective setting, with $J = 10$ being a more aggressive noise-removal setting, and $J = 1$ being a

setting which retains more data. Since noise increases with total energy, a threshold based on observed significant waveheight, $E_n(H_{m0})$ is used rather than a fixed E_n. This anti-noise algorithm is described in the Appendix.
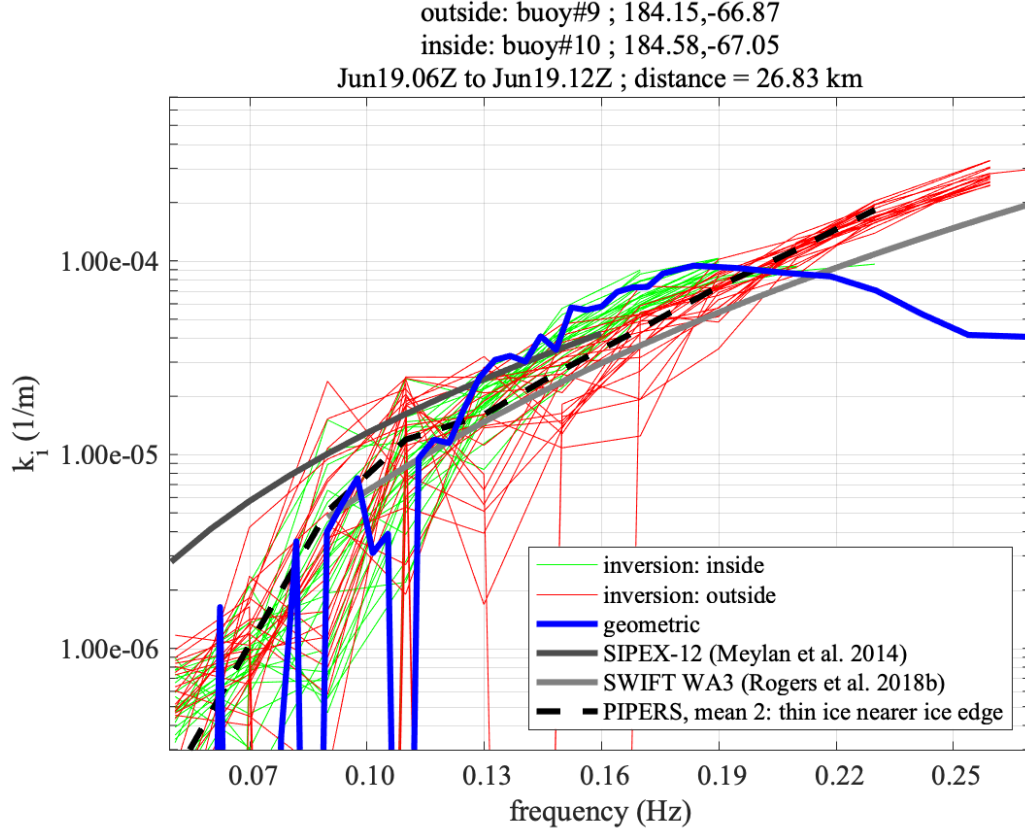

Figure 5. Estimated dissipation rates, as a function of frequency ("dissipation profiles", $k_i(f)$), comparing the inversion results (thin green and red lines) against the results from the simple geometric method (thick blue line). Grey and black lines are reference profiles. See text for explanation.

6. Inversion results (dissipation profiles)

This section discusses the $k_i(f)$ profiles resulting from the application of the inverse method to the PIPERS dataset. The overall goal is to identify the correlation between the $k_i(f)$ profiles and other variables. Since k_i and frequency are the primary and secondary variables presented, and these other variables are referred to here as "tertiary variables".

6.1. Methods: co-located variables (tertiary parameters)

In this section, we list the tertiary variables which we will inspect for correlation with $k_i(f)$ profiles from the inversions.

Ice concentration, a_{ice} estimates are taken from AMSR2 and are the same fields as used in the model forcing (Section 4.2).

16

Ice thickness, h_{ice} estimates are derived from the MIRAS radiometer onboard the European Space Agency's SMOS satellite. Processed files are provided by the Univ. Bremen (https://seaice.uni-bremen.de/thin-ice-thickness/), Huntemann et al. (2014) and Paţilea et al. (2019). These files are on a 12 km polar stereographic grid, with one analysis per day. Ice thickness (h_{ice}) values are available at ice thicknesses up to 50 cm, where the instrument saturates. Therefore, cases of h_{ice}=50 cm presented here should be interpreted as h_{ice}>=50 cm. In cases where the daily field is missing, the h_{ice} value is flagged as unusable.

Ice distance, x_{ice} is computed as the distance from the buoy to the ice edge. Since the buoys are in ice, the algorithm searches for the nearest open water point ($a_{ice} = 0$). Isolated open water points are disregarded.

Significant waveheight, H_{m0}. This parameter is taken from buoy observations. H_{m0} is computed as $H_{m0} = 4\sqrt{m_0}$, where $m_n = \int E(f)f^n df$, and $E(f)$ is the one dimensional (non-directional) energy spectrum, and the bounds of integration are defined by the overlap with model spectral range, i.e. 0.042 to 0.476 Hz.

Seven other tertiary variables are described in the Supplemental Information and included in the associated Mendeley Data archive[2]: mean period, T_m; fourth spectral moment, m_4; significant steepness, S_{sig}; representative orbital velocity, V; wind speed, U_{10}; air temperature; and date.

Our purpose here is to identify correlations. These correlations may or may not indicate causal relations. A number of these variables are computed from the wave spectrum itself (H_{m0}, T_m, m_4, S_{sig}, and V). If the relationship is causal, this implies *nonlinearity* of the dissipation. Such behavior would not be extraordinary, e.g. whitecapping dissipation S_{wc} is *extremely* nonlinear, and in fact, we already use a few nonlinear forms of S_{ice} in WW3, e.g. the dissipation by ice-water friction under orbital motion as implemented by F. Ardhuin in Stopa et al. (2016, Appendix B) and some of the empirical forms implemented by Collins and Rogers (2017). Extensive discussion of potential nonlinearity of S_{ice} can be found in Squire (2018).

6.2. Methods: Quantifying role of tertiary parameters

We use inversion results from the nine buoys in the eastern group (see Section 3) during the period of 6 to 30 June, and only consider cases with a_{ice}>0.22. This results in 9477 valid k_i profiles. In the cases where h_{ice} is the tertiary parameter, the population is reduced further, to only include the 8957 k_i profiles with contemporaneous h_{ice} estimates, see Section 6.1.

Given our objective to reveal dependency on the tertiary variables, the intuitive approach would be to sort and bin the $k_i(f)$ profiles according to the associated values of the tertiary parameters. However, this approach results in spurious flattening of the profiles, as will be discussed in Section 6.3. Instead, the $k_i(f)$ profiles are sorted and binned according to the length of the $k_i(f)$ profiles in frequency space. Naively, we should not expect this to reveal trends associated with the tertiary variables. However, since our anti-noise algorithm terminates the profiles in a way

---

[2] The 9477 dissipation profiles, energy-to-noise estimates E/E_n, and co-located tertiary variables can be downloaded from Mendeley Data, http://dx.doi.org/10.17632/5b742jv7t5.1 .

that is strongly correlated with the tertiary variables, this approach does in fact yield indirect sorting on these variables, and so we can identify a clear correlation of $k_i(f)$ with the tertiary variables, without the spurious flattening.

6.3. Results

Figure 6 shows the results, with each bin-averaged $k_i(f)$ profile colored according to the mean of the tertiary parameter within that bin population. This is given in four panels, one for each of the four tertiary variables (h_{ice}, a_{ice}, x_{ice}, H_{m0}). The gray rectangle in each panel indicates the first two frequency bins of the inversion. As noted in Section 5, the inversion results for this frequency range are potentially most affected by errors in boundary forcing. The number of $k_i(f)$ profiles used in each mean $k_i(f)$ profile (colored lines in Figure 6) varies, e.g. with 785, 2334, and 118 profiles being used for mean profiles terminating at 0.07, 0.11, and 0.23 Hz, respectively. Four reference profiles are shown in Figure 6: the "SIPEX" and "SWIFT" reference profiles (solid gray and black lines) were introduced in Section 5. The two PIPERS reference profiles are based on a simple mean of all profiles, which will be denoted as "mean 1" and a mean of profiles in thinner ice nearer the ice edge, described in Section 7, "mean 2".
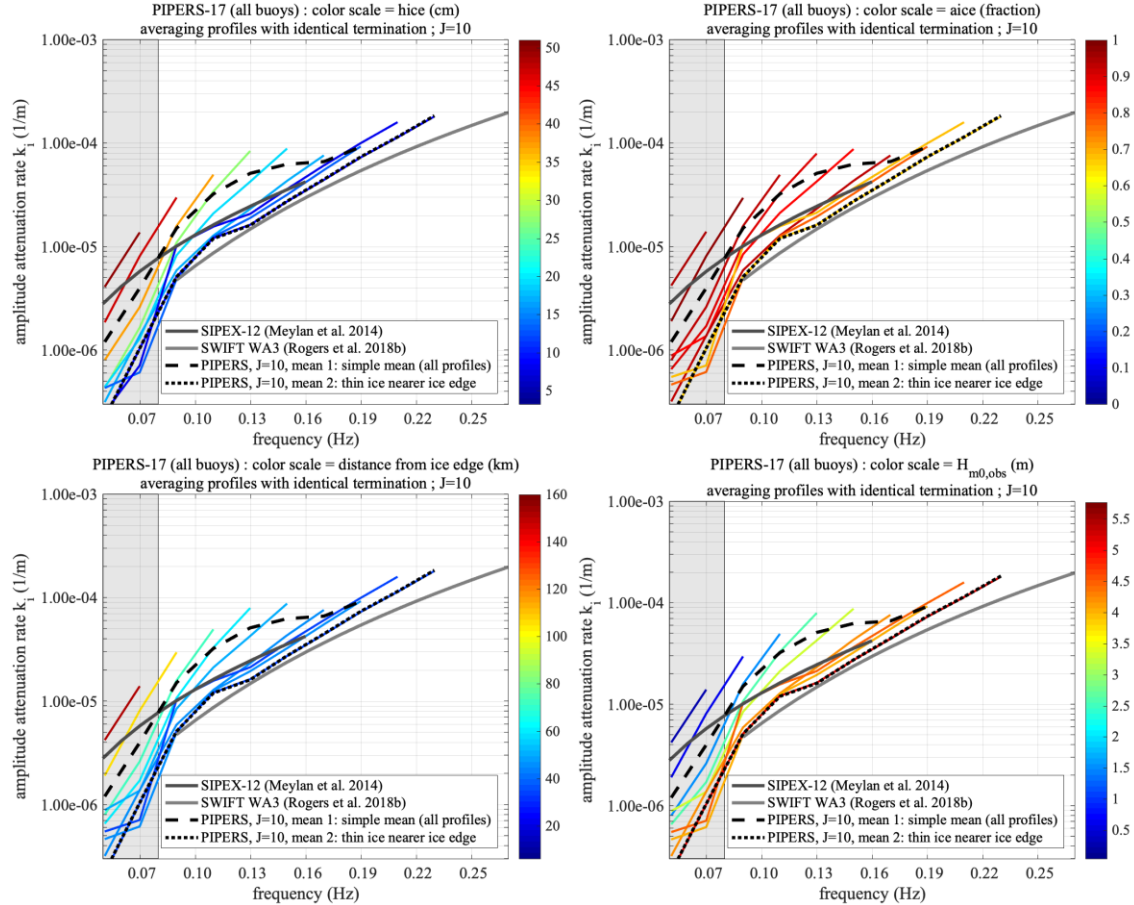
Figure 6. Dissipation profiles estimated using the model-data inversion with a conservative anti-noise algorithm (J=10). Four variables are evaluated here: ice thickness, ice concentration, distance from ice edge, and significant waveheight. Reference profiles (gray and black lines) and the gray-shaded rectangle are explained in the text.

Some noteworthy features of Figure 6 are:

1) With ice concentration, a_{ice}, there is a weak trend for lower dissipation with lower ice concentration. Plotted mean values of a_{ice} vary from 0.67 to 0.98. The k_i plotted here is the dissipation of only the ice-covered fraction of the sea. We scale S_{ice} by ice concentration in the model, $S_{ice} = -2a_{ice}C_g k_i E$.
2) Across all frequencies ($f \leq 0.23$ Hz), there is a clear increase in $k_i(f)$ with h_{ice}. This is an intuitively causal relation and is consistent with a primary conclusion of Robin (1963), who observed that ice thickness is the most useful parameter to predict the penetration of waves into sea ice for lower frequencies ($f<0.10$ Hz).
3) Unsurprisingly, the dependence on x_{ice} is broadly similar to the dependence on h_{ice}. (There is thicker ice farther from the ice edge.)
4) There is a clear trend of smaller $k_i(f)$ for larger waveheight, H_{m0}. This may be coincidental since larger waves occur closer to the ice edge, or it may be causal. A possible causal relation would be the breakup of floes during large events, making the ice cover more pliable and less dissipative. This is a nonlinear type of dissipation. Considering the ice cover as quasi-viscous in aggregate, this is a thixotropic behavior (shear thinning) and is reversed from the more typical nonlinearity for wave model dissipation terms, e.g. higher dissipation for larger orbital velocity, or larger steepness, etc. This correlation is consistent with the results of Montiel et al. (2018), who find that for larger waveheights ($H_{m0}> 3$ m), k_i is inversely proportional to H_{m0} (i.e. linear, non-exponential decay).

Discussion: Flattening of dissipation profiles

The approach used here—bin-averaging based on termination frequency—was not the first that we applied. Rogers et al. (2020) used the more intuitive approach: to sort and bin the $k_i(f)$ profiles according to the associated values of the tertiary parameters. However, that study found spurious results associated with flattening of the $k_i(f)$ profiles. This flattening can be thought of as a nascent or more subtle variation on the "roll-over" effect noticed in observational data by Wadhams et al. (1988) and others. In fact, Wadhams et al. (1988) themselves offer the possibility that this non-monotonic behavior is an artifact of non-representation of wind input. This, and other, possible causes of flattening are reviewed by Rogers et al. (2020). Here, we focus on two causes that we believe are most important to our analysis.

Flattening can be caused by averaging of $k_i(f)$ profiles which terminate at different frequencies. The "mean 1" profile (dashed black line in Figure 6), which is just a simple mean of all $k_i(f)$ values, is an example of this. In lower frequencies, say up to 0.14 Hz, the mean is dominated by high-dissipation profiles which terminate at these frequencies, while in mid-frequencies, say from 0.14 to 0.23, the mean is dominated by smaller-dissipation profiles which extend into these frequencies. This artifact affects the "mean 1" profile but does not affect the colored (binned) profiles presented in Figure 6, or "mean 2" profile, since all $k_i(f)$ profiles used in each averaging terminate at the same frequency.

Anything that tends to "prop up" the high-frequency portion of the spectrum will contribute to flattening or even roll-over of $k_i(f)$. As discussed in Section 3 and Thomson et al. (2020), instrument noise has this tendency. Given our aggressive removal of k_i values with possible

noise contamination using J=10, (Section 5), this problem is unlikely to affect results shown in Figure 6. However, it is useful to evaluate this aggressive strategy. After all, with a less aggressive anti-noise algorithm, the binned profiles extend farther in frequency space, a desired feature. Results using the less conservative value of J=1 are shown in Figure 7. This indicates that though the flattening is slight with J=1, it does unmistakably occur. In other words, the use of J=10 appears to be justified.

The above suggests an interesting paradox: exclusion of noise-contaminated data prevents artificial flattening of individual $k_i(f)$ profiles; but this "fix" —i.e. early termination of profiles—itself results in artificial flattening of mean profiles, if those means are calculated using dissimilar termination frequencies.
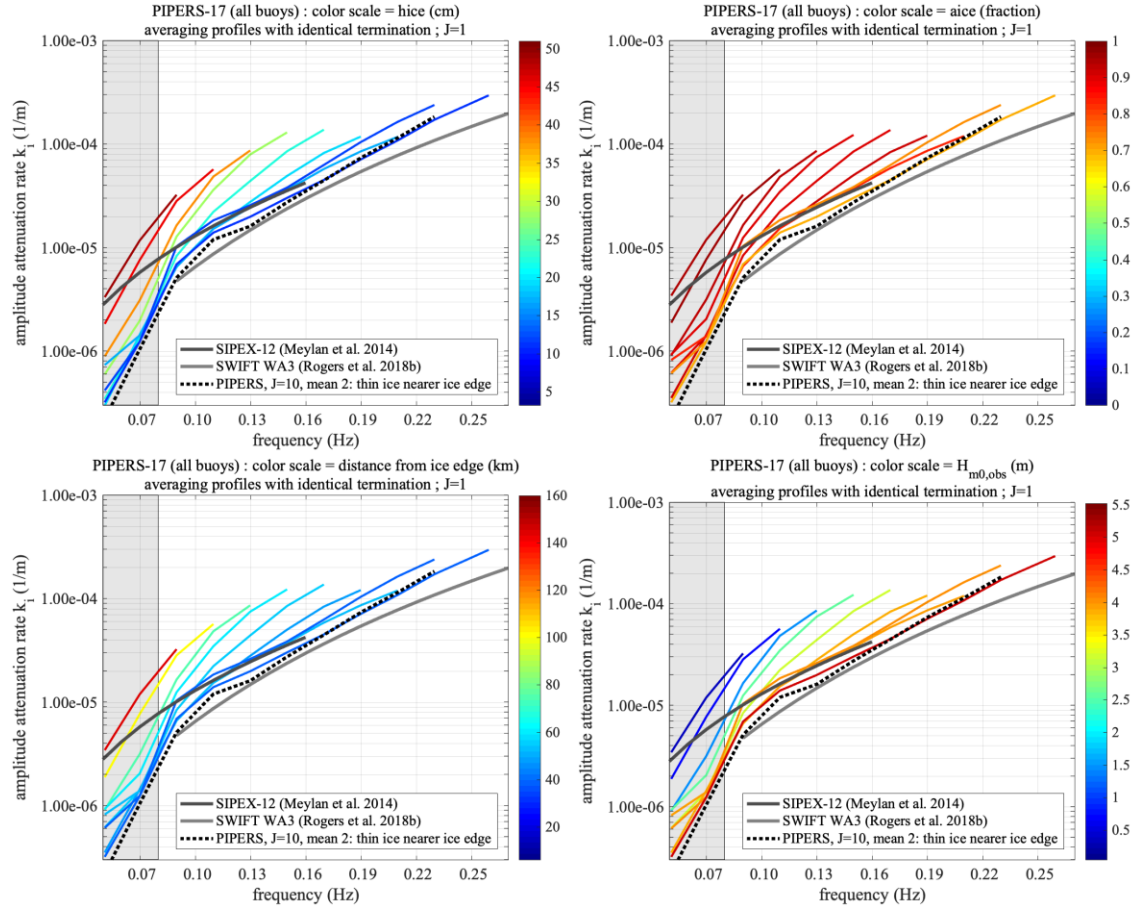
Figure 7. Like Figure 6, but using a less aggressive setting for the anti-noise algorithm: J=1.

7. Fitting to parametric model

Empirically-derived mean k_i profiles can be fitted to a parametric form. Several possible forms exist, but here, we look at monomial and binomial subsets of the general polynomial $k_i = \sum C_n f^n$. This follows the approach of Meylan et al. (2014), who used $C_2 f^2 + C_4 f^4$, i.e. $n = 2$ and 4. The value of n can be interpreted as an indicator of a dominant physical process (or two processes in the case of a binomial) if they match the n predicted by a theoretical model. For

example, if an empirical k_i profile fits well to $n = 7$; this would support the argument that dissipation is caused by something like viscosity in the ice layer (Keller model, see Section 2).

Herein, we use two methods of creating mean profiles. Neither extends beyond 0.23 Hz, since the number of valid $k_i(f)$ values at higher frequencies is relatively small, due to the omission of $k_i(f)$ estimates that may be affected by noise (Section 5). Both are created using the more aggressive anti-noise algorithm, J=10. The two methods are:

1) A "simple mean" profile, denoted "mean 1" in this text. As long as a $k_i(f)$ value is considered valid; it is included in the average. As with the binned profiles in Figure 6, the mean profile excludes frequencies for which the population of the frequency bin is less than 5% of the maximum, and so the profile terminates at 0.19 Hz. As an example, this averaging includes 8739, 2715, and 664 k_i values at bins centered at 0.09, 0.15, and 0.19 Hz respectively.
2) A mean using only the profiles which span the full frequency space of the mean profile (0.051 to 0.23 Hz in terms of bin centers) and only cases with thinner ice (h_{ice} <14 cm) and those nearer the ice edge (x_{ice} <63 km). This averaging thus includes only 116 profiles but provides greater consistency within the averaging and uniformity of population. This averaging is denoted "M2" (mean 2).

The top left panel of Figure 8 shows the mean k_i profile M2 on log-log scale, so that the slopes of the line segments correspond to values of n. Integer values of n are indicated as straight lines on these panels. The mean profile has mean slope slightly less than $n = 4$ for the range 0.09 to 0.23 Hz. Various tested binomials and monomials were tested, summarized in Table 2, and we find the best outcome using a binomial fit of $n = 2$ and 4, but nearly the same accuracy using a monomial fit to $n = 3.5$ to 4.

The top right panel of Figure 8 illustrates the error minimization process used to find the best fit values of C_n for the $n = 2$ and 4 binomial. The diagonal error distribution suggests that the dependence is distributed between the two terms of the binomial. Best fit coefficients are given in Table 2. The first two bins are excluded during the fitting process, since inversion results are more sensitive to errors in boundary forcing for these bins. Goodness-of-fit is quantified by root-mean-square error (RSME), where the error is $\log_{10}(k_{i,fit}) - \log_{10}(k_{i,M2})$ and M2 denotes mean 2.

Dependence on $n = 2$ to 4 can be found in several theoretical models reviewed in Section 2, namely: two new theoretical models of Meylan et al. (2018) ($n = 2$ and $n = 3$), the turbulent boundary layer model ($n = 3$), the Robinson and Palmer (1990) model ($n = 3$), the inextensible surface cover model ($n = 3.5$), and the Kohout et al. (2011) friction model ($n = 4$). Though notably, most of these models do not predict the dependence of dissipation on ice thickness, h_{ice}.

The mean profile and fitted polynomial of M2 is shown in the lower panel of Figure 8, along with the mean profile "mean 1", and k_i estimates from prior studies. The quality of fit is excellent. The power dependence (i.e. slope) is consistent with previous analyses using different datasets: the M2 binomial is compared to earlier binomial fits, from Meylan et al. (2014) and Rogers et al. (2018b). The M2 binomial fit is lower than that from Meylan et al. (2014) (for broken floes near Antarctica) by factors from 0.45 to 0.93 in the 0.08 to 0.16 Hz range, and is higher than that from Rogers et al. (2016) (for pancake and frazil ice near the Beaufort Sea) by

factors from 1.07 to 1.44 in the 0.09 to 0.23 Hz range. We also plot the k_i estimates for low frequency waves from Ardhuin et al. (2016) for an energetic swell case near Svalbard in ice of thickness 2 to 4 m. At these frequencies, (f <0.08 Hz) the simple mean of PIPERS suggests a weaker dissipation than the Ardhuin estimates, which is unsurprising given the much thinner ice during the PIPERS experiment.

Limitations

Because in the underlying dataset there is variance about the mean profiles, any simple parametric model that is only a function of frequency will have limited skill, even when directly applied to the same case. Inclusion of tertiary variables, such as h_{ice}, in the parametric formula is a logical next step.
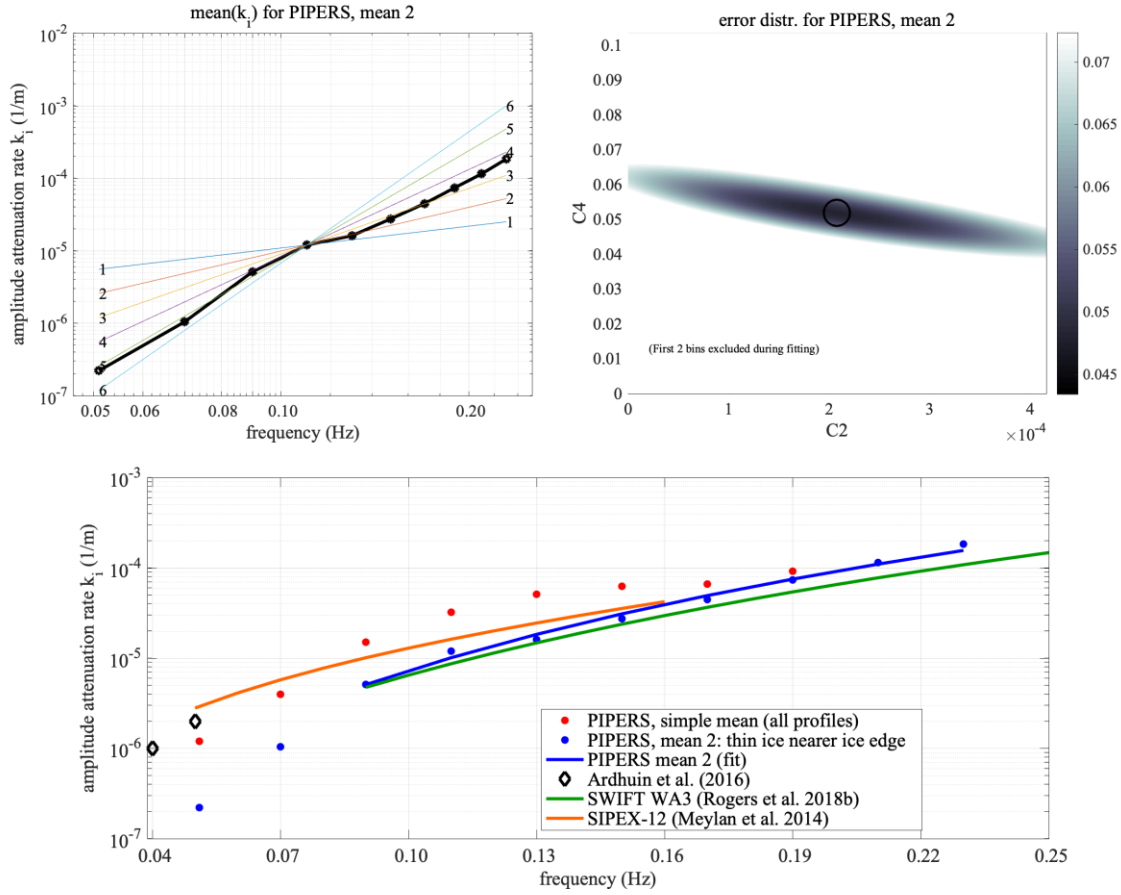
Figure 8. Top: Power fit for "mean 2" from this study. Top left: Evaluation of power dependence of k_i on frequency. Power dependence corresponds to fixed slope on this log-log scale. Integers within axes indicate power dependence. Top right: Error surface for determining best-fit coefficients. Bottom: Comparison to other estimates of $k_i(f)$. See text for further explanation.

Table 2. Best fit coefficients for binomials and monomials of the form $k_i(f) = C_A f^{n_A} + C_B f^{n_B}$. The first row corresponds to the binomial fitting shown in Figure 8. Calculation of RMSE is explained in the text.

n_A	C_A	n_B	C_B	RMSE
2	2.08e-4	4	5.18e-2	0.048
3	2.83e-3	4	4.31e-2	0.052
3	9.52e-3	0	0	0.107
3.25	1.52e-2	0	0	0.081
3.5	2.43e-2	0	0	0.061
3.75	3.89e-2	0	0	0.055
4	6.22e-2	0	0	0.067

8. Summary and Conclusions

In this section, we summarize the study, list the conclusions based on the analysis presented, and lastly, we offer thoughts and speculations about the results.

Summary

- A new dataset is presented: $k_i(f)$ profiles (dissipation rate as a function of frequency) from model/data inversion. These are computed using observations of waves in ice in the Southern Ocean: the "PIPERS" dataset presented by Kohout et al. (2020). Here, 24 days (6 to 30 June 2017) are used. This is a subset of the larger dataset and includes 9477 $k_i(f)$ profiles.
- The model/data inversion method is a relatively new method for estimating dissipation rate, and is particularly appropriate to this field study because it does not require that the buoy configuration is aligned with the mean wave direction: in the PIPERS field study, buoys became misaligned over time due to drift.
- The $k_i(f)$ profiles are evaluated by studying their correlation with four environmental variables (denoted "tertiary variables"): ice concentration a_{ice}, distance from ice edge x_{ice}, ice thickness h_{ice} and significant waveheight H_{m0}. This multi-dimensional analysis is made possible by the large population of the dataset (9477).
- The $k_i(f)$ profiles are presented using a novel method of binning which quantifies correlation with the tertiary parameters.
- Two mean $k_i(f)$ profiles are computed, and a parametric model of dissipation are created by fitting to the mean that is based on profiles of thinner ice found nearer the ice edge.

Conclusions

- Results indicate a positive correlation between dissipation rate $k_i(f)$ and ice thickness h_{ice}.
- Results indicate a negative correlation between dissipation rate $k_i(f)$ and waveheight, H_{m0}.

- The simple mean of all $k_i(f)$ values, denoted "mean 1", exhibits a flattening in higher frequencies (0.13 to 0.19 Hz) that is spurious, resulting from averaging profiles with dissimilar termination frequencies. This type of averaging is therefore not recommended.
- The second mean of $k_i(f)$ profiles, denoted "M2" and representing cases of thinner ice closer to the ice edge. This profile is well described by a binomial using $n = 2$ and 4, or by a monomial using n between 3.5 and 4.
- The binomial for M2 is qualitatively similar to the binomials from Meylan et al. (2014) and Rogers et al. (2018). The former was computed for a case of broken floes in Antarctica using simple geometric calculations, and is higher than M2 by a ratio of 1.07 to 2.24. The latter was computed using an inversion with wind input scaling, for an example of pancake and frazil ice in the western Arctic, and these values are generally lower than those of M2, by factors 0.69 to 0.93.
- We tested two possible settings for an algorithm to eliminate data contaminated by instrument noise and find that when the less conservative setting is used, there is a slight, spurious flattening of some $k_i(f)$ profiles near their terminal frequencies, an outcome predicted by Thomson et al. (2020).

Further discussion

- Power dependence found here (n =2 to 4) can be compared with our review of power dependence in the literature (Section 2). For example, $n = 3.5$ dependence is consistent with an existing model for dissipation caused by friction with laminar flow at the ice-water interface, and $n = 4$ is consistent with another friction model, Kohout et al. (2011).
- The negative correlation between dissipation rate and energy may be coincidental rather than causal. If causal, it follows the analog to a thixotropic (shear-thinning) ice cover.
- Further, this negative correlation apparently contradicts formulae which assume that dissipation increases with orbital velocity. However, the correlation does not isolate for coincident variables and so is inconclusive.
- Variability of the 9477 $k_i(f)$ profiles estimated here is significant. Any parametric dissipation rate that is only a function of frequency, $k_i(f)$, applied in a forward model—even for the same case shown here—can be expected to be accurate only in the mean sense. Correlations with tertiary variables such as h_{ice} found here may be exploited in the development of new parametric dissipation formulae and applied in predictive models.

Acknowledgments

based ice thickness estimates. We thank Mr. Michael Phelps (NRL Oceanography Division contractor) for providing archives of the NAVGEM fields. We thank Drs. David Wang (NRL), Jim Thomson (UW/APL), and Tripp Collins (USACE) for helpful information and advice about instrument error and data processing.

This is NRL contribution number NRL/JA/7320-20-4950 and is approved for public release.

Appendix: Noise threshold

An algorithm was developed for this study, to remove $E(f)$ records for which noise contributes significantly to $E(f)$, specifically $E(f) < JE_n$, where E_n is the estimated noise level and J is a subjective setting (Section 5).

Traditionally, instrument noise most severely affects the measurement of long, low-amplitude waves. For example, if the acceleration spectrum measured by a buoy is contaminated by noise that is uniform in frequency (white noise), then the contamination of $E(f)$ will fall off at a slope of f^{-4}, and tend to be extremely small at higher frequencies, relative to an open water spectrum. However, in sea ice, the high-frequency $E(f)$ is much lower than an open water spectrum, such that noise may be a significant portion of $E(f)$. As noted in our discussion of Figure 3, the high-frequency tail appears to be "propped up", and this may be caused by noise. We conservatively assume that this feature *is* caused by noise, and seek to exclude contaminated data. This requires an automated estimate of E_n.

Instrument noise is expected to increase with total energy, so our approach is designed to include this dependency. The development was initiated by sorting spectra by significant waveheight H_{m0} and organizing in groups of 50, so the first group has 50 spectra with the lowest H_{m0}, and so on. The groups were then manually evaluated to estimate the $E(f)$ below which the spectra are visibly contaminated, similar to Figure 3. In a second phase, an objective method was created, following these steps:

1) For each group of 50 spectra, a mean spectrum was computed. The averaging was performed in log-space.
2) The slope of the mean spectrum was computed, in log-log space.
3) The point in frequency space where the negative slope in the tail was steepest was identified. This is assumed to be the point where dissipation by sea ice is very strongly suppressing the tail while noise is negligible.
4) The point in frequency space where the magnitude of slope reaches less than 55% of the maximum is identified. This is treated as the noise level E_n. The criterion of 55% was determined as the setting which most closely matches the subjective (manual) evaluation.
5) Since the spectra were sorted by H_{m0} prior to grouping, the computed thresholds were then available as $E_n = E_n(\langle H_{m0} \rangle)$, where $\langle H_{m0} \rangle$ is the mean H_{m0} of each group. We then performed a least-squares fit linear regression to $E_n(\langle H_{m0} \rangle)$ in log-log space, resulting in a power fit, $E_n = 3.99 \times 10^{-4} H_{m0}^{0.85}$.

Since a different accelerometer was used for buoys 13 and 14, we perform a separate analysis for these buoys, giving $E_n = 3.89 \times 10^{-3} H_{m0}^{1.86}$. These represent only 550 out of the 9477 spectra, so a smaller group size (20) was used for these buoys. The two fits are illustrated in Figure A1.

The overall outcome of applying the algorithm is that for cases further from the ice edge, the $k_i(f)$ profiles terminate at lower frequency (i.e. more data is discarded). This is because $E(f)$ is more strongly damped (pushed down toward E_n) further from the ice edge. At the same time, the dependence of our noise floor on waveheight implies a lower E_n further from the ice edge. This empirically-determined dependence works against the overall outcome above but is not strong enough to reverse it.
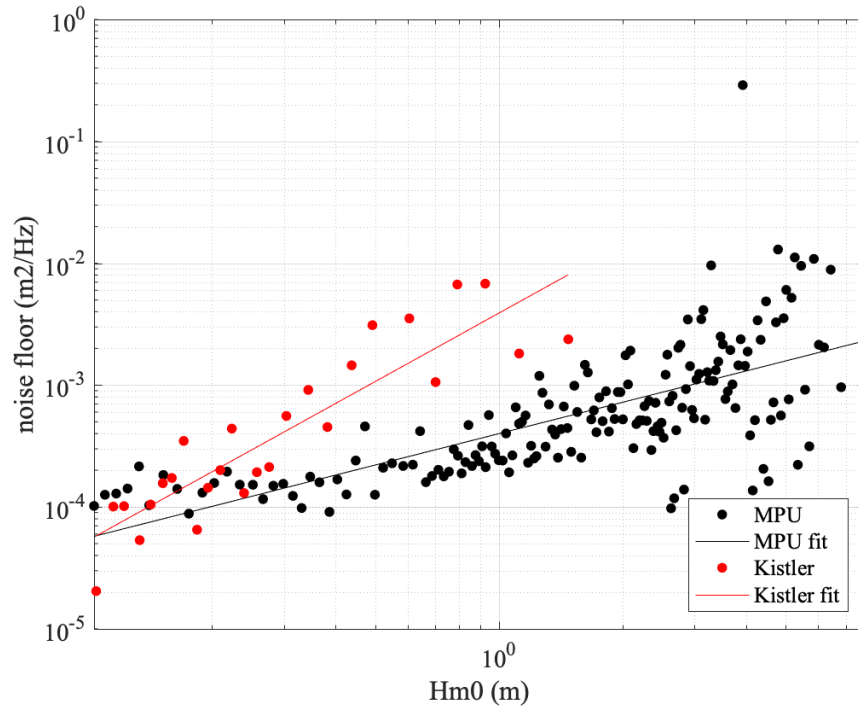

Figure A1. Noise level E_n as a function of waveheight. Dots indicate results using the algorithm based on spectral slope. Lines indicate power fits. "MPU" and "Kistler" denote two types of accelerometers used. "MPU" accounts for 94.2% of the measured spectra, and "Kistler" represents the other 5.8% (buoys 13 and 14).

Data Availability

The PIPERS wave spectra can be downloaded from ftp://ftp.niwa.co.nz/incoming/Kohout/WII_2017 or obtained by contacting Alison.Kohout@niwa.co.nz. Dissipation profiles presented here are available from Mendeley Data, http://dx.doi.org/10.17632/5b742jv7t5.1. Other data files used to create figures herein are available from the corresponding author by request.

References

Alberello, A., Onorato, M., Bennetts, L., Vichi, M., Eayrs, C., MacHutchon, K., and Toffoli, A., 2019. Brief communication: Pancake ice floe size distribution during the winter expansion of the Antarctic marginal ice zone, *The Cryosphere*, **13**, 41–48, https://doi.org/10.5194/tc-13-41-2019.

Ardhuin, F., Rogers, W. E., Babanin, A.V., Filipot, J.-F., Magne, R., Roland, A., van der Westhuysen, A., Queffeulou, P., Lefevre, J.-M., Aouf, L. and Collard, F., 2010. Semi-

empirical dissipation source functions for ocean waves: Part I, definitions, calibration and validations, *J. Phys. Oceanogr.* **40**, 1917-1941.

Ardhuin, F., P. Sutherland, M. Doble, and P. Wadhams, 2016. Ocean waves across the Arctic: Attenuation due to dissipation dominates over scattering for periods longer than 19 s, *Geophys. Res. Lett.,* **43**, 5775–5783, doi:10.1002/2016GL068204.

Asplin, M.G.; J. Marko, D.B. Fissel, K. Borg, 2018. Investigating Propagation of Short-Period Ocean Waves into the Periphery of Arctic Pack Ice Using High-Resolution Upward-Looking Sonar, *Atmosphere-Ocean*, 56 (3), 152-161, https://doi.org/10.1080/07055900.2018.1498765.

Beitsch, A., L. Kaleschke, S. Kern, and X. Tian-Kunze, 2013. AMSR2 ASI 3.125 km Sea Ice Concentration Data, V0.1, Institute of Oceanography, University of Hamburg, Germany, digital media. (ftp-projects.zmaw.de/seaice/).

Beitsch, A., L. Kaleschke, and S. Kern, 2014. Investigating High-Resolution AMSR2 Sea Ice Concentrations during the February 2013 Fracture Event in the Beaufort Sea, *Remote Sens.*, **6**, 3841-3856

Bennetts, L.G., Williams, T.D., 2015. Water wave transmission by an array of floating discs. *Proc. R. Soc. A*, 471:20140698

Bennetts L.G., O'Farrell, S., Uotila, P., 2017. Brief communication: impacts of ocean-wave-induced breakup of Antarctic sea ice via thermodynamics in a stand-alone version of the CICE sea-ice model, *Cryosphere*, 11:1035–40

Bidlot, J., 2018. Intercomparison of operational wave forecasting systems against buoys: September to November 2017, Report for The Joint WMO-IOC Technical Commission for Oceanography and Marine Meteorology (JCOMM), 90 pp., retrieved from http://www.jcomm.info/wave on 8 April 2020.

Boutin, G., Ardhuin, F., Dumont, D., Svigny, C., Girard-Ardhuin, F., Accensi, M., 2018. Floe size effect on wave-ice interactions: possible effects, implementation in wave model, and evaluation. *J. Geophys. Res. Oceans* **123**, 4779–805

Cavaleri, L., S. Abdalla, A. Benetazzo, L. Bertotti, J.R. Bidlot, Ø. Breivik, S. Carneil, R.E. Jensen, J.P. Yandum, W.E. Rogers, A. Roland, A. Sanchez- Arcilla, J.M. Smith, J. Staneva, Y. Toledo, G.Ph. van Vledder, and A.J. van der Westhuysen, 2018: Wave modelling in coastal and inner seas. *Progress in Oceanography,* **167,** 164-233, https://doi.org/10.1016/j.pocean.2018.03.010.

Cheng, S., W.E. Rogers, J. Thomson, M. Smith, M.J. Doble, P. Wadhams, A.L. Kohout, B. Lund, O.P.G. Persson, C.O. Collins III, S.F. Ackley, F. Montiel and H.H. Shen, 2017. Calibrating a Viscoelastic Sea Ice Model for Wave Propagation in the Arctic Fall Marginal Ice Zone. *J. Geophys. Res.,* **122** doi://10.1002/2017JC013275

Collins, C.O., and W.E. Rogers, 2017. A Source Term for Wave Attenuation by Sea ice in WAVEWATCH III®: IC4, *NRL Report NRL/MR/7320--17-9726*, 25 pp. [available from www7320.nrlssc.navy.mil/pubs.php].

Collins, C., M. Doble, B. Lund, and M. Smith, 2018. Observations of surface wave dispersion in the marginal ice zone. *J. Geophys. Res.,* **123**. doi:10.1029/2018JC01378.

Doble, M. J., 2009. Simulating pancake and frazil ice growth in the Weddell Sea: A process model from freezing to consolidation, *J. Geophys. Res.*, **114**, C09003, doi:10.1029/2008JC004935.

Doble, M. J., and P. Wadhams, 2006. Dynamical contrasts between pancake and pack ice, investigated with a drifting buoy array, *J. Geophys. Res.*, 111, C11S24, doi:10.1029/2005JC003320.

Doble, M. J. and Bidlot, J.-R., 2013. Wavebuoy measurements at the Antarctic sea ice edge compared with an enhanced ECMWF WAM: progress towards global waves-in-ice modeling, *Ocean Model.*, **70**, 166-173, doi:10.1016/j.ocemod.2013.05.012.

Doble, M. J., De Carolis, G., Meylan, M.H., Bidlot, J.-R. and Wadhams, P., 2015. Relating wave attenuation to pancake ice thickness, using field measurements and model results, *Geophys. Res. Lett.*, 42, 4473-4481, doi:10.1002/2015GL063628.

Elgar, S., 1987. Bias of effective degrees of freedom of a spectrum, *J. Waterway, Port, Coastal, and Ocean Eng.,* **113**(1)*,* 77-82.

Gemmrich, J., W.E. Rogers, J. Thomson, and S. Lehner, 2018: Wave evolution in off-ice wind conditions *J. Geophys. Res.: Oceans,* **123**, 5543–5556, https://doi.org/10.1029/2018JC013793.

Hasselmann, S., Hasselmann, K., Allender, J.H. and Barnett, T.P., 1985. Computations and parameterizations of the nonlinear energy transfer in a gravity-wave spectrum. Part II: Parameterizations of the nonlinear energy transfer for application in wave models. *J. Phys. Oceanogr.*, 15, 1378-1391.

Herman, A., Cheng, S., and Shen, H.H., 2019. Wave energy attenuation in fields of colliding ice floes – Part 1: Discrete-element modelling of dissipation due to ice–water drag, *The Cryosphere*, 13, 2887–2900, https://doi.org/10.5194/tc-13-2887-2019.

Hogan, T., and 16 Coauthors, 2014. The Navy Global Environmental Model. *Oceanogr.,* **27**(3), 116-125.

Huntemann, M., Heygster, G., Kaleschke, L., Krumpen, T., Mäkynen, M., and Drusch, M., 2014. Empirical sea ice thickness retrieval during the freeze-up period from SMOS high incident angle observations, *The Cryosphere*, **8**, 439-451, doi:10.5194/tc-8-439-2014.

Keller, J.B.,1998. Gravity waves on ice-covered water. *J. Geophys. Res.*, **103** (C4): 7663-7669.

Kohout, A.L., Williams, M., 2019. Antarctic wave-ice observations during PIPERS. NIWA client report 2019060CH prepared for the Deep South Challenge. National Institute of Water and 470 Atmospheric Research, New Zealand. Contact: library@niwa.co.nz.

Kohout, A.L., M.H. Meylan, D.R. Plew, 2011. Wave attenuation in a marginal ice zone due to the bottom roughness of ice floes. *Annals of Glaciology*, **52**(57), 118-122.

Kohout, A. L., M. J. M. Williams, S. M. Dean, and M. H. Meylan, 2014. Storm-induced sea-ice breakup and the implications for ice extent, *Nature,* **509***,* 604–607.

Kohout, A. L., B. Penrose, S. Penrose, M.J.M. Williams, 2015. A device for measuring wave-induced motion of ice floes in the Antarctic marginal ice zone. *Annals of Glaciology,* **56** (69), 415-424.

Kohout, A.L., Smith, M., Roach, L.A., Williams, G., Montiel, F., Williams, M.J.M., 2020. Observations of exponential wave attenuation in Antarctic sea ice during the PIPERS campaign. *Annals of Glaciology*, 1–14. https://doi.org/10.1017/aog.2020.36

Lamb, H., 1932. *Hydrodynamics*. Sixth Edition. New York, Dover Publications, 768 pp.

Li, J., S. Mondal, H.H. Shen, 2015a. Sensitivity analysis of a viscoelastic parameterization for gravity wave dispersion in ice covered seas. *Cold Reg. Sci. Technol*. **120**, 63–75.

Li, J., Kohout, A.L., and Shen, H.H., 2015b. Comparison of wave propagation through ice covers in calm and storm conditions, *Geophys. Res. Lett.* **42**(14)*,* 5935–5941, doi: 10.1002/2015GL064715.

Li, J., Kohout, A. L., Doble, M. J., Wadhams, P., Guan, C., and Shen, H. H., 2017. Rollover of apparent wave attenuation in ice covered seas. *J. Geophys. Res.*, **122**. https://doi.org/10.1002/2017JC012978.

Liu, A.K. and E. Mollo-Christensen, 1988. Wave propagation in a solid ice pack. *J. Phys. Oceanogr.*, **18**, 1702-1712.

Liu, Q., Rogers, W. E., Babanin, A. V., Young, I. R., Romero, L., Zieger, S., Qiao, F. and Guan, C., 2019. Observation-based source terms in the third-generation wave model WAVEWATCH III: updates and verification, *J. Phys. Oceanogr*. 49. 489-517.

Liu, Q., Rogers, W.E., Babanin, A., Li, J., and Guan, C., 2020. Spectral modelling of ice-induced wave decay, *J. Phys. Oceanogr.*, https://doi.org/10.1175/JPO-D-19-0187.1

Marchenko, A., Wadhams, P., Collins, C., Rabault, J., Chumakov, M., 2019. Wave-ice interaction in the north-west Barents Sea. *Appl. Ocean Res.* 90, 101861. ISSN 0141-1187. https://doi.org/10.1016/j.apor.2019.101861.

Meylan, M., L.G. Bennetts, and A.L. Kohout, 2014. In situ measurements and analysis of ocean waves in the Antarctic marginal ice zone, *Geophys. Res. Lett.*, **41**, 5046–5051, doi:10.1002/2014GL060809.

Meylan, M.H., Bennetts, L.G., Mosig, J.E.M., Rogers, W.E., Doble, M.J. and Peter, M.A., 2018. Dispersion relations, power laws, and energy loss for waves in the marginal ice zone, *J. Geophys. Res*., 123, 3322-3335. https://doi.org/10.1002/2018JC013776.

Montiel F, Squire V.A., Bennetts L.G., 2016. Attenuation and directional spreading of ocean wave spectra in the marginal ice zone. *J. Fluid Mech.* **790**, 492–522.

Mosig, J.E.M., F. Montiel, and V.A. Squire, 2015. Comparison of viscoelastic-type models for ocean wave attenuation in ice-covered seas, *J. Geophys. Res.*, **120**, 6072–6090, doi:10.1002/2015JC010881.

Montiel, F., Squire, V.A., Doble, M.J., Thomson, J., Wadhams, P., 2018. Attenuation and directional spreading of ocean waves during a storm event in the autumn Beaufort Sea marginal ice zone. *J. Geophys. Res.*, **123**, 5912–32

Orzech, M., Shi, F., Veeramony, J., Bateman, S., Calantoni, J., and Kirby, J., 2016. Incorporating floating surface objects into a fully dispersive surface wave model, *Ocean Model.*, 102, 14–26, https://doi.org/10.1016/j.ocemod.2016.04.007.

Pațilea, C., Heygster, G., Huntemann, M., and Spreen, G., 2019. Combined SMAP–SMOS thin sea ice thickness retrieval, *The Cryosphere*, 13, 675–691, https://doi.org/10.5194/tc-13-675-2019.

Rabault, J., Sutherland, G., Jensen, A., Christensen, K.H., Marchenko, A., 2019. Experiments on wave propagation in grease ice: Combined wave gauges and PIV measurements. *J. Fluid Mech.* 864, 876–898. https://doi.org/10.1017/jfm.2019.16

Roach L.A., Smith, M.M., Dean S.M., 2018. Quantifying growth of pancake sea ice floes using images from drifting buoys. *J. Geophys. Res. Oceans* 123:2851–66.

Robin, G.Q., 1963. Wave propagation through fields of pack ice. *Philosophical Transactions of the Royal Society of London. Series A, Mathematical and Physical Sciences*, **255**(1057), 313-339.

Robinson, N. J., and S. C. Palmer, 1990. A modal analysis of a rectangular plate floating on an incompressible liquid, *J. Sound Vibration*, **142**(3), 453–460, doi:10.1016/0022-460X(90)90661-I.

Rogers, W.E. and R.S. Linzell, 2018. The IRI Grid System for Use with WAVEWATCH III. *NRL Report NRL/MR/7320--18-9835*, 47 pp. [available from www7320.nrlssc.navy.mil/pubs.php]

Rogers, W.E., J. Thomson, H.H. Shen, M.J. Doble, P. Wadhams and S. Cheng, 2016. Dissipation of wind waves by pancake and frazil ice in the autumn Beaufort Sea, *J. Geophys. Res.*, **121,** 7991-8007, doi:10.1002/2016JC012251.

Rogers, W.E., P. Posey, L. Li, R. A. Allard, 2018a. Forecasting and hindcasting waves in and near the marginal ice zone: Wave modeling and the ONR "Sea State" field experiment. *NRL Report NRL/MR/7320--18-9786*, 179 pp. [available from www7320.nrlssc.navy.mil/pubs.php].

Rogers, W.E., M.H. Meylan, A.L. Kohout, 2018b. Frequency distribution of dissipation of energy of ocean waves by sea ice using data from Wave Array 3 of the ONR "Sea State" field experiment. *NRL Report NRL/MR/7322--18-9801*, 25 pp. [available from www7320.nrlssc.navy.mil/pubs.php].

Rogers, W.E., Meylan, M.H., Kohout, A.L., Estimates of dissipation of wave energy by sea ice for a field experiment in the Southern Ocean, using model/data inversion, 2020. *arXiv eprint*, published online 8 June 2020, https://arxiv.org/abs/2006.04978 .

Shen, H.H., 2019. Modelling ocean waves in ice-covered seas, *Applied Ocean Res.*, **83**, doi:10.1016/j.apor.2018.12.009.

Shi, Y.F., Yang, Y.Z., Teng, Y., Sun, M., Shengjun, Y., 2019. Mechanism of sea ice formation based on comprehensive observation data in Liaodong Bay, China. *J. of Oceanol. and Limn.*, 37 (6): 1846-1856, https://doi.org/10.1007/s00343- 019-8269-8.

Spreen, G., L. Kaleschke, G. Heygster, 2008. Sea Ice Remote Sensing Using AMSR-E 89 GHz Channels, *J. Geophys. Res.*, **113**, C02S03, doi:10.1029/2005JC003384.

Squire, V.A., 1998. "The Marginal Ice Zone", in Physics of Ice-covered Seas, Vol. 1, edited by Matti Lepparanta, Helsinki University Printing House, Helsinki, 381-446.

Squire VA., 2018. A fresh look at how ocean waves and sea ice interact. *Philos. Trans. R. Soc. A* 376:20170342, 13 pp.

Squire, V. A., 2020. Ocean wave interactions with sea ice: a reappraisal, *Annual Rev. Fluid Mech.* 52, 37–60.

Sree, D.K.K., A.W.-K. Law, H.H. Shen, 2018. An experimental study on gravity waves through a floating viscoelastic cover, *Cold Reg. Sci. Technol.*, https://doi.org/10.1016/j.coldregions.2018.08.01

Stopa, J.E., F. Ardhuin, F. Girard-Ardhuin, 2016. Wave climate in the Arctic 1992-2014: seasonality and trends, *The Cryosphere*, **10**, 1605-1629.

Stopa, J. E., Sutherland, P., and Ardhuin, F., 2018. Strong and highly variable push of ocean waves on Southern Ocean sea ice, *P. Natl. Acad. Sci. U.S.A.*, 115, 5861–5865.

Sutherland, G., Rabault, J., Christensen, K.H., Jensen, A., 2019. A two layer model for wave dissipation in sea ice. *Appl. Ocean Res.* 88, 111–118. ISSN 0141-1187. https://doi.org/10.1016/j.apor.2019.03.023.

Sutherland, P., J. Brozena, W.E. Rogers, M. Doble and P. Wadhams, 2018. Airborne remote sensing of wave propagation in the marginal ice zone *J. of Geophys. Res.: Oceans*, 123, 4132-4152, https://doi.org/10.1029/2018JC013785.

Thomson, J., 2012. Wave breaking dissipation observed with "SWIFT" drifters, *J. Atmos. Ocean. Tech.,* **29**, 1866–1882, doi:10.1175/JTECH-D-12-00018.1.

Thomson, J. and 32 co-authors, 2018. Overview of the Arctic Sea State and Boundary Layer Physics Program, *J. Geophys. Res.*, 8674-8687, doi:10.1002/2018JC013766.

Thomson, J., Hosekova, L., Meylan, M.H., Kohout, A.L., Kumar, N., 2020. Spurious rollover of wave attenuation rates in sea ice caused by noise in field measurements, *ESSOAr preprint*, published online 22 July 2020, https://doi.org/10.1002/essoar.10503733.1 .

Toffoli, A., Bennetts, L.G., Meylan, M.H., Cavaliere, C., Alberello, A., Elsnab, J., Monty, J. P., 2015. Sea ice floes dissipate the energy of steep ocean waves. *Geophys. Res. Lett.* 42:8547–54.

Tolman, H.L., 1991. A Third-generation model for wind-waves on slowly varying, unsteady, and inhomogeneous depths and currents, *J. Phys. Oceanogr.* **21**(6*),* 782-797.

Vichi, M., Eayrs, C., Alberello, A., Bekker, A., Bennetts, L., Holland, D., et al., 2019. Effects of an explosive polar cyclone crossing the Antarctic marginal ice zone. *Geophys. Res. Lett.*, 46. https://doi.org/10.1029/2019GL082457

Voermans, J., Babanin, A., Thomson, J., Smith, M., and Shen, H., 2019. Wave attenuation by sea ice turbulence, *Geophys. Res. Lett.*, 46, 6796–6803, https://doi.org/10.1029/2019GL082945.

Wadhams, P., 1978. Wave decay in the marginal ice zone measured from a submarine. *Deep-Sea Res.*, 25, 23-40.

Wadhams, P., Squire, V.A., Goodman, D.J., Cowan A.M. and Moore, S.C., 1988. The attenuation rates of ocean waves in the marginal ice zone, *J. of Geophys. Res*., 93, 6799-6818.

WAVEWATCH III® Development Group (WW3DG), 2016. User manual and system documentation of WAVEWATCH III® version 5.16. *Tech. Note 329*, NOAA/NWS/NCEP/MMAB, College Park, MD, U.S.A., 326 pp. + Appendices.

Weber, J.E., 1987. Wave attenuation and wave drift in the marginal ice zone. *J. Phys. Oceanogr*., **17**(12), 2351-2361.

Worby, A. P. (1999), Observing Antarctic Sea Ice: A practical guide for conducting sea ice observations from vessels operating in the Antarctic pack ice. A CD-ROM produced for the Antarctic Sea Ice Processes and Climate (ASPeCt) program of the Scientific Committee for Antarctic Research (SCAR) Global Change (GLOCHANT) program, Hobart, Tasmania, Australia. See also: http://aspect.antarctica.gov.au/ , (retrieved 6 April 2020)

Yue C., Li, J.K., Guan, C.L., Lian, X.H., Wu, K.J., 2019. Surface wave simulation during winter with sea ice in the Bohai Sea. *J. of Oceanol. and Limn.*, 37 (6): 1 857-1 867, https://doi.org/10.1007/s00343- 019-8253-3.

Zhao, X., Cheng, S., Shen, H.H., 2017. Nature of wave modes in a coupled viscoelastic layer over water. *J. Eng. Mech.* 143:04017114.

Supporting information for
"Estimates of spectral wave attenuation in Antarctic sea ice, using model/data inversion"

W. Erick Rogers, Naval Research Laboratory, Stennis Space Center, MS, USA

Michael H. Meylan, The University of Newcastle, Australia

Alison L. Kohout, National Institute of Water and Atmospheric Research (NIWA), New Zealand

Corresponding author: W. Erick Rogers (erick.rogers@nrlssc.navy.mil)

Table of Figures

Animation

In addition to these figures, an animation is provided, "`nest_M14.gif`", which shows results similar to those shown in Figure 4 of the paper. In this animation, we use the "IC4M2" parameterization (see WW3 user manual), with the Meylan et al. (2014) binomial for the S_{ice} source function. This animation is not provided with the intent to compare against the observations, since that is not the purpose of the paper. Rather, it is provided to provide context of wave conditions during the experiment, as well as the buoy positions during the 24-day period of the study.
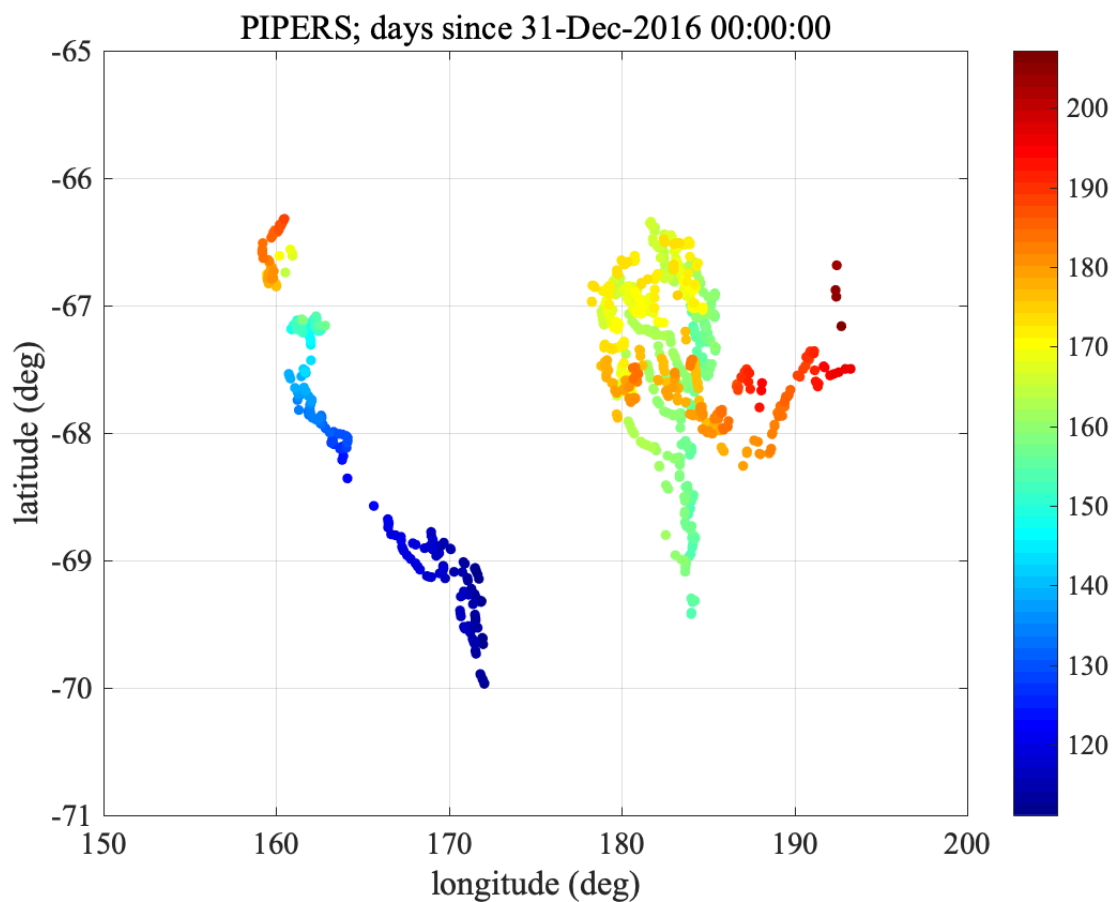
Figure 1. Buoy tracks for the entire PIPERS buoy deployment, showing the positions with respect to time. Colors indicate year-day during 2017.

positions from 06-Jun-2017 00:00:00 to 30-Jun-2017 00:00:00
red=9 ; blue=10 ; magenta=7 ; green=6 ; cyan=5 ; black=14
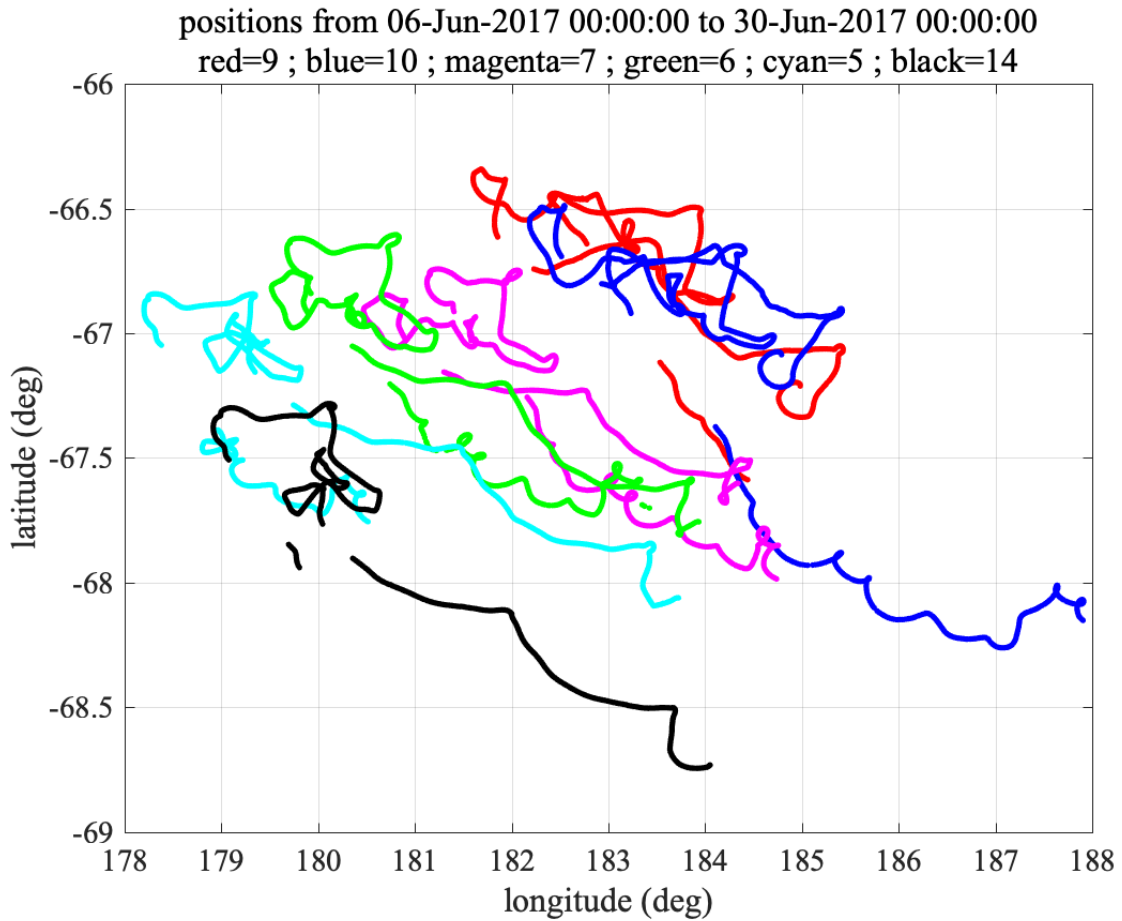
Figure 2. Buoy tracks for the time period used in the paper, 2017 June 6 to 30, indicating the buoy numbers of the six buoys used in Table 1 and Figures 2, 3, and 4 of the main text, using the same color scheme as is used in those figures.
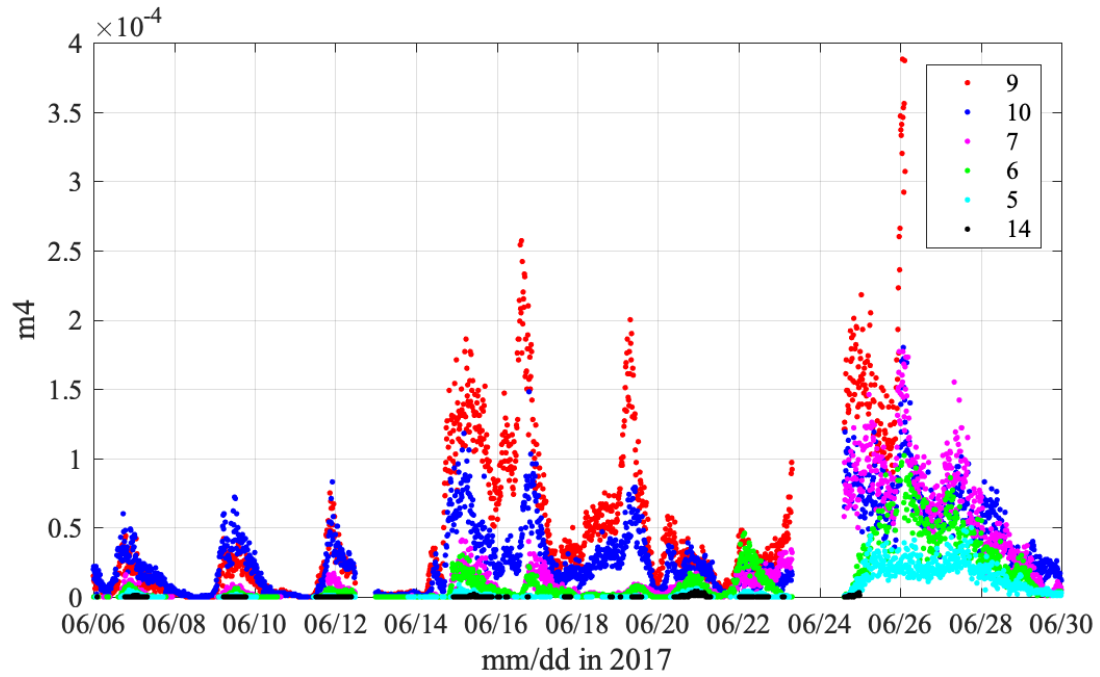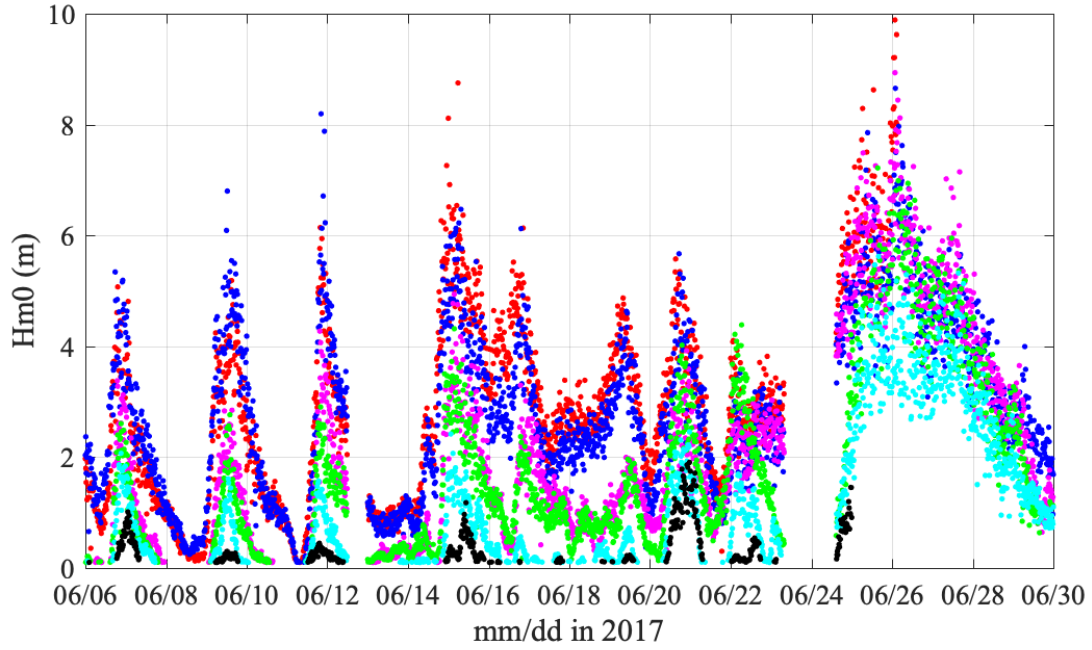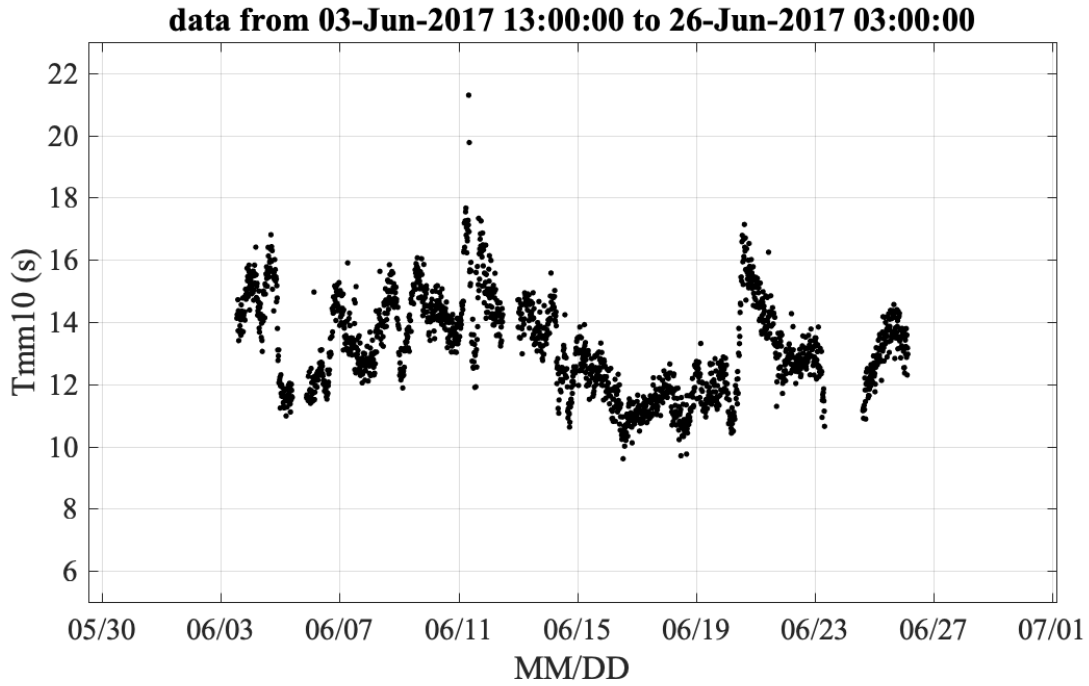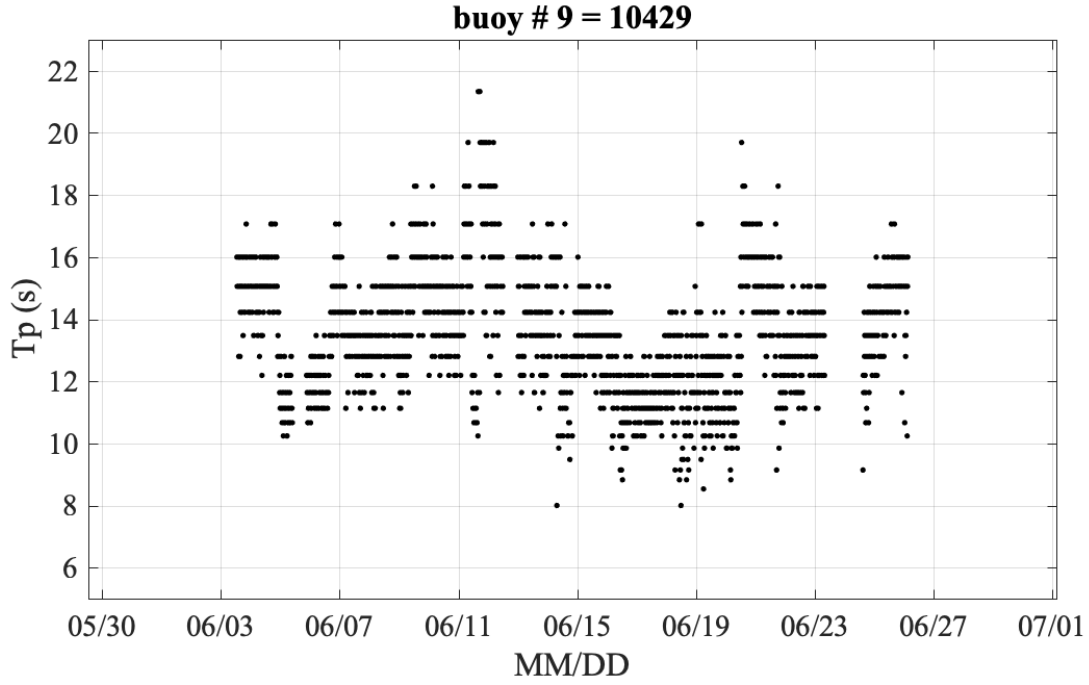
Figure 3. Waveheight (H_{m0}) and m_4 time series for the six buoys used in Table 1 and Figures 2, 3, and 4 of the main text, using the same color scheme as is used in those figures.

buoy # 9 = 10429

data from 03-Jun-2017 13:00:00 to 26-Jun-2017 03:00:00

Figure 4. Peak period and mean period $T_{m,-1,0}$ for buoy 9. This buoy is near the ice edge, thus this figure is an indication of the dominant wave period of incident waves during the experiment. Since this buoy is in the ice, where some low-pass filtering is occurring, the unmeasured wave periods outside the ice (north of the buoy) may be slightly shorter.

1.1. Methods: co-located variables (tertiary parameters)

In this section, we list the tertiary variables which we will inspect for correlation with $k_i(f)$ profiles from the inversions. These variables are also included in the Mendeley Data archive, http://dx.doi.org/10.17632/5b742jv7t5.1.

Ice concentration, a_{ice} estimates are taken from AMSR2 and are the same fields as used in the model forcing (see main article).

Ice thickness, h_{ice} estimates are derived from the MIRAS radiometer onboard the European Space Agency's SMOS satellite. Processed files are provided by the Univ. Bremen and downloaded from https://seaice.uni-bremen.de/thin-ice-thickness/ . These files are on a 12 km polar stereographic grid, with one analysis per day. Ice thickness (h_{ice}) values are available at ice thicknesses up to 50 cm, where the instrument saturates. Therefore, cases of h_{ice}=50 cm presented here should be interpreted as h_{ice}>=50 cm. In cases where the daily field is missing, the h_{ice} value is flagged as unusable. The reader is referred to Huntemann et al. (2014) and Paţilea et al. (2019) for more information about the SMOS "thin sea ice" thickness retrieval.

Ice distance, x_{ice} is computed as the distance from the buoy to the ice edge. Since the buoys are in ice, the algorithm searches for the nearest open water point ($a_{ice} = 0$). Isolated open water points are disregarded. This estimate is approximate insofar as it is not necessarily the distance along the main axis of wave propagation.

Significant waveheight, H_{m0}. This parameter is taken from buoy observations. H_{m0} is computed as $H_{m0} = 4\sqrt{m_0}$, where $m_n = \int E(f)f^n df$, and $E(f)$ is the one dimensional (non-directional) energy spectrum, and the bounds of integration are defined by the overlap with model spectral range, i.e. 0.042 to 0.476 Hz.

Mean period, T_m. This parameter is taken from buoy observations. This is more precisely denoted as $T_{m,-1,0}$, computed as $T_{m,-1,0} = m_{-1}/m_0$. The parameter is preferred over peak period because of its superior stability, but is typically close to, or slightly below, the peak period.

Spectral fourth moment, m_4. This is $m_4 = \int E(f)f^4 df$, also taken from buoy observations. The parameter is proportional to the "low pass mean square slope", $s_{lp}^2 = m_4(2\pi)^4/g^2 \sim 16.2 m_4$ (S.I. units), where g is the gravitational acceleration. This parameter is included because, being a higher order moment, it is sensitive to energy level at higher frequencies, and thus is strongly affected by sea ice.

Significant steepness, S_{sig}. This is also taken from buoy observations and is defined here as $S_{sig} = H_{m0}/L_m$, where L_m is the mean wavelength, computed from $T_{m,-1,0}$. Given deep water, $L_m = 1.56 T_{m,-1,0}^2$ (S.I. units). This parameter is included based on the hypothesis that wave steepness may correlate with the condition of the sea ice, e.g. existence of relatively steep waves may be an indication that the ice has been broken into relatively small floes.

Representative orbital velocity, V. This is also taken from buoy observations, defined as $V = (H_{m0}/T_{m,-1,0})(\pi/\sqrt{2})$. This follows from the open water definition of orbital velocity excursion at the surface: $V = a_{rms}\sigma$, where $a_{rms} = \sqrt{2m_0}$ and $\sigma = 2\pi/T$. This parameter is included based on the hypothesis that, if S_{ice} is associated with turbulence caused by friction at the ice-water interface, then it may correlate with the velocity of orbital motion at the water surface. The open water definition is used for the sake of simplicity.

Wind speed, U_{10}. This is the magnitude of the NAVGEM 10-m wind vectors used in the model forcing (see main article).

Air temperature, T_{air}. This is taken from the NAVGEM surface air temperature fields corresponding to the 10-m wind vectors used in the model forcing (see main article). This parameter is included based on the hypothesis that, insofar as new ice growth is affected by air temperature, the ice conditions may correlate with air temperature. This is more specifically targeting the formation of frazil ice in the open water fraction of the region considered.

Date. Though this parameter cannot have a direct causal link to $k_i(f)$, it is included as a tertiary parameter in the Mendeley data archive, since there are many possibilities for indirect effects, as the ice/ocean/atmosphere climate changes during this late autumn to early winter period.

Our purpose here is to identify correlations. These correlations may or may not indicate causal relations, i.e. direct dependence of $k_i(f)$ on the tertiary variable.

1.2. Correlation with tertiary parameters (Figures)

Figure for the four tertiary variables, a_{ice}, h_{ice}, x_{ice} and , H_{m0} are given in the main text. Six other variables are plotted here: T_m, m_4, S_{sig}, V, U_{10}, and T_{air}. Date is not plotted, since shifts in "mean date" would be primarily associated with the time sequence of buoy failures, i.e. not physically meaningful.
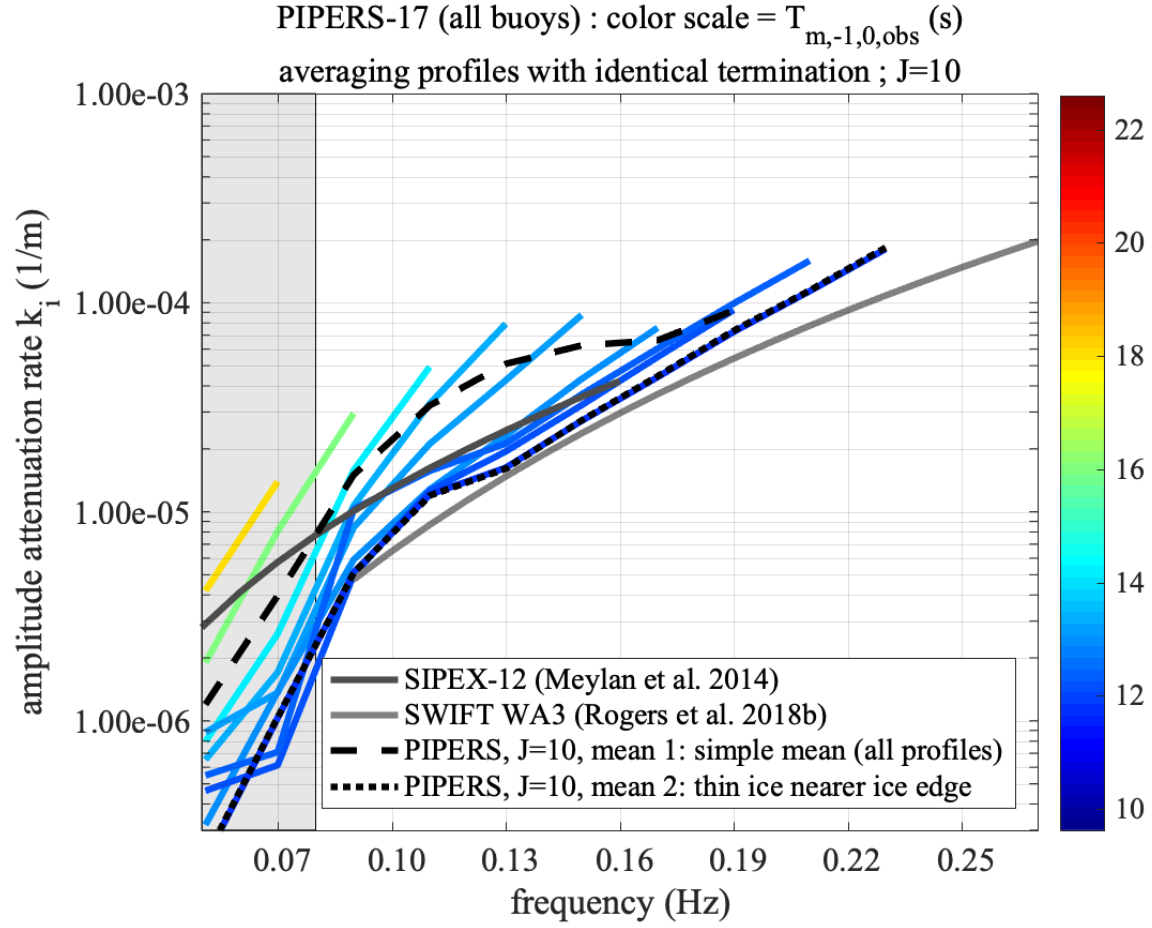
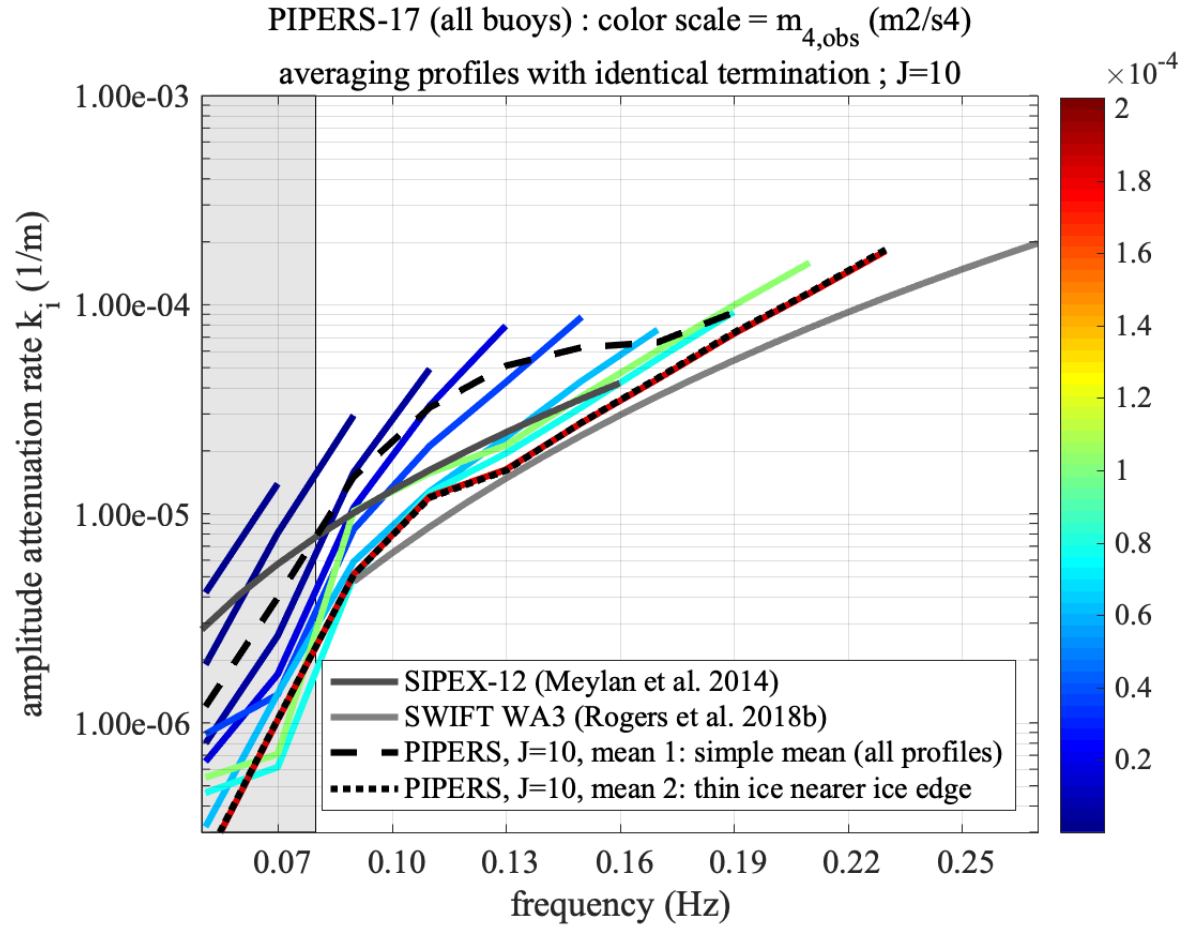Figure 5. Like Figure 6 of the main text, except showing T_m.

Figure 6. Like Figure 6 of the main text, except showing m_4.
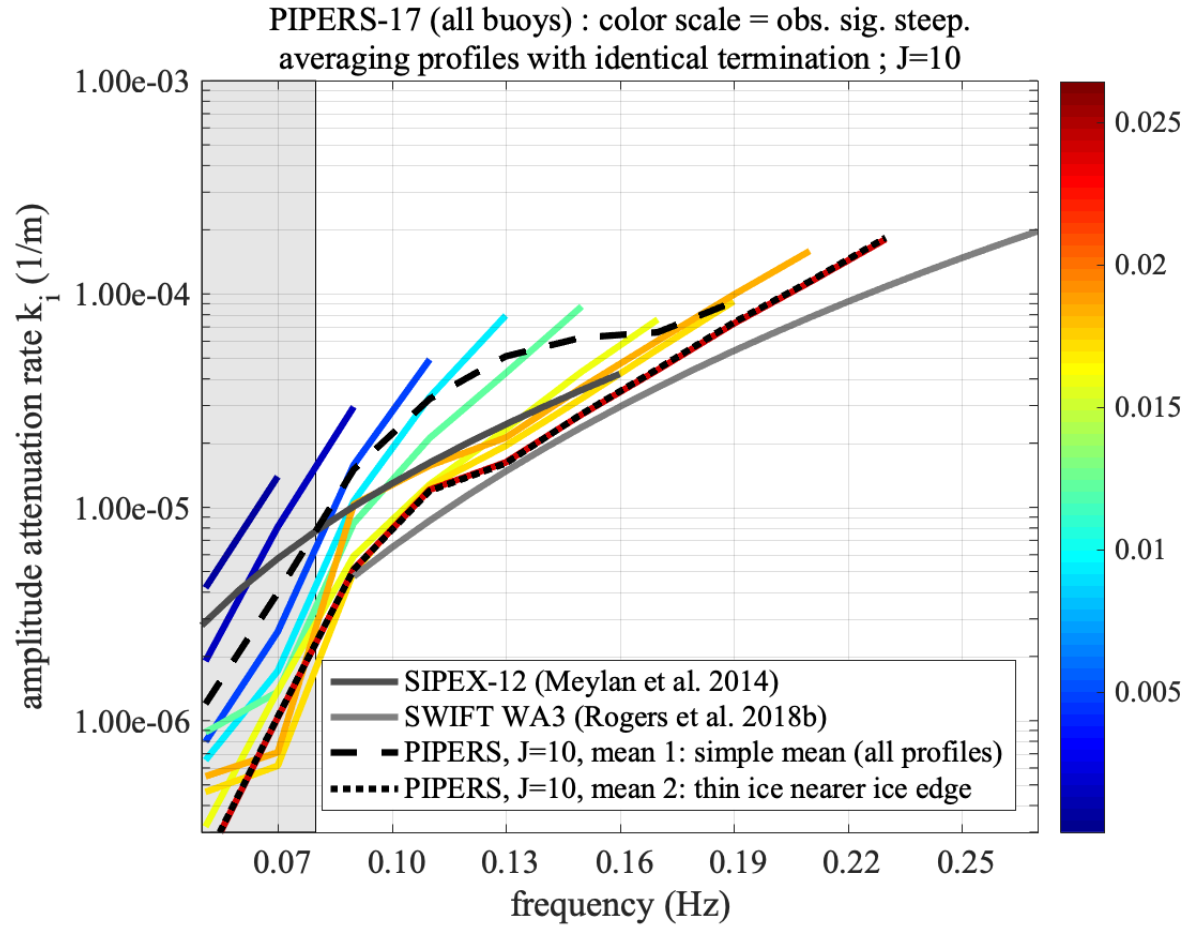
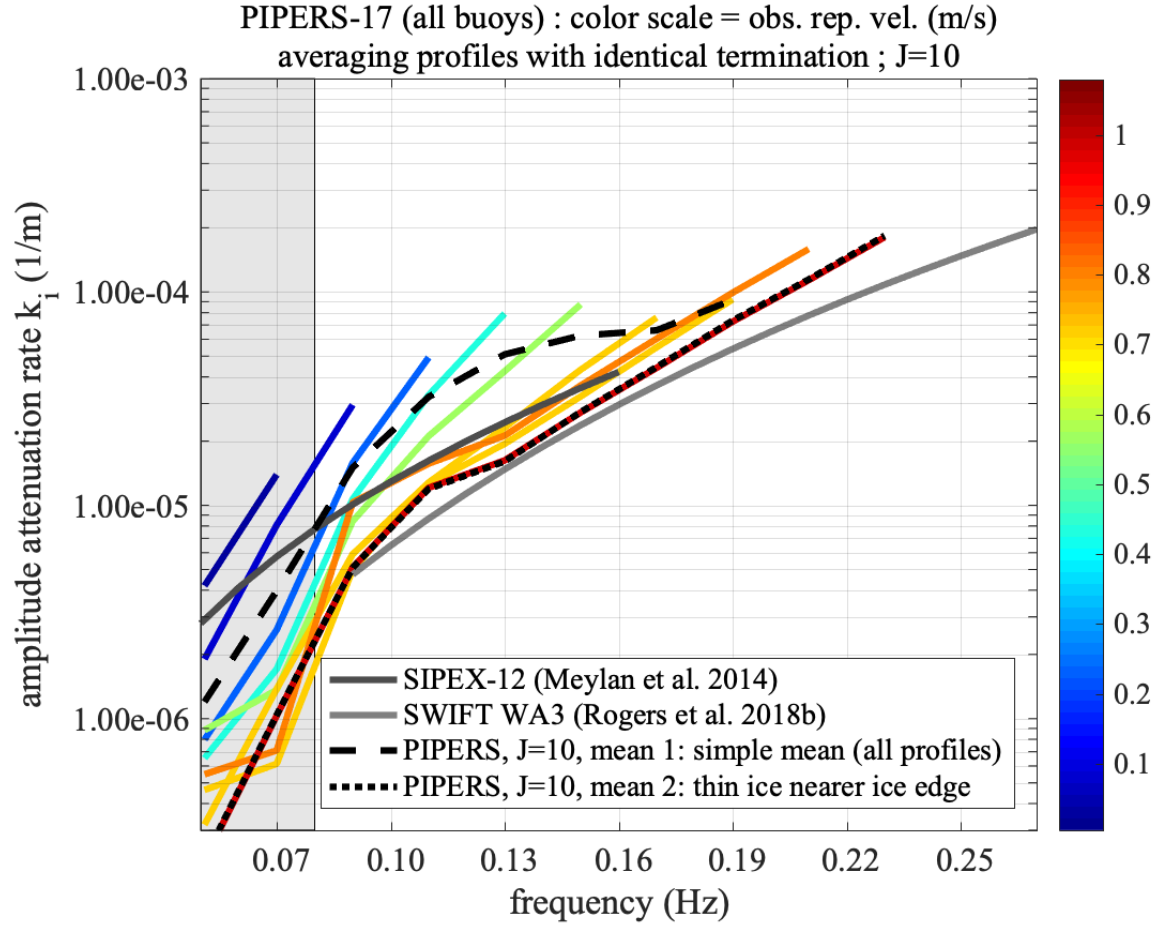Figure 7. Like Figure 6 of the main text, except showing S_{sig}.

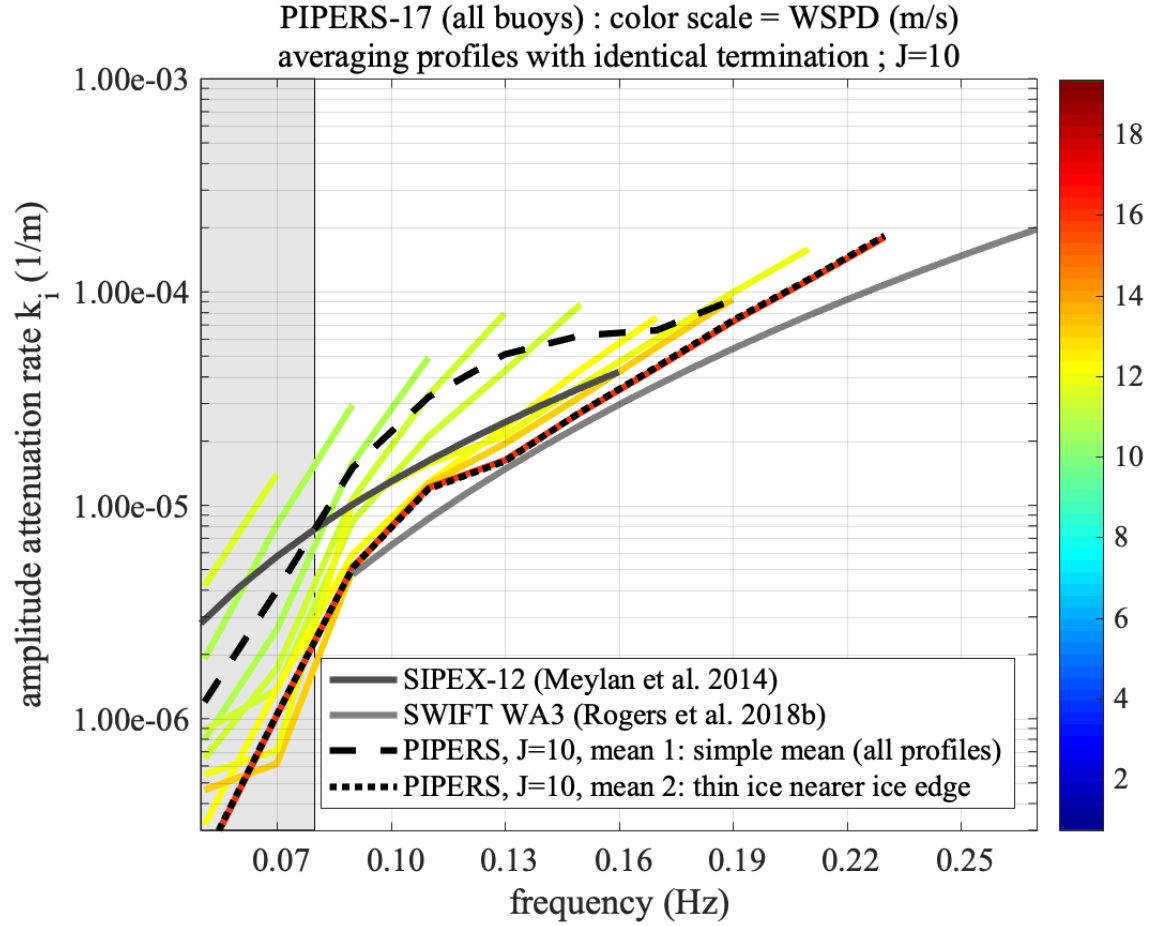Figure 8. Like Figure 6 of the main text, except showing V.

Figure 9. Like Figure 6 of the main text, except showing U_{10}. In this figure and other correlation figures, the mean $k_i(f)$ profile terminating at 0.23 Hz represents cases for which $E(0.23 \text{ Hz}) > 10E_n$. The mean wind speed for this case is 16.1 m/s. Other mean $k_i(f)$ profiles have mean wind speeds from 10.8 to 13.0 m/s.
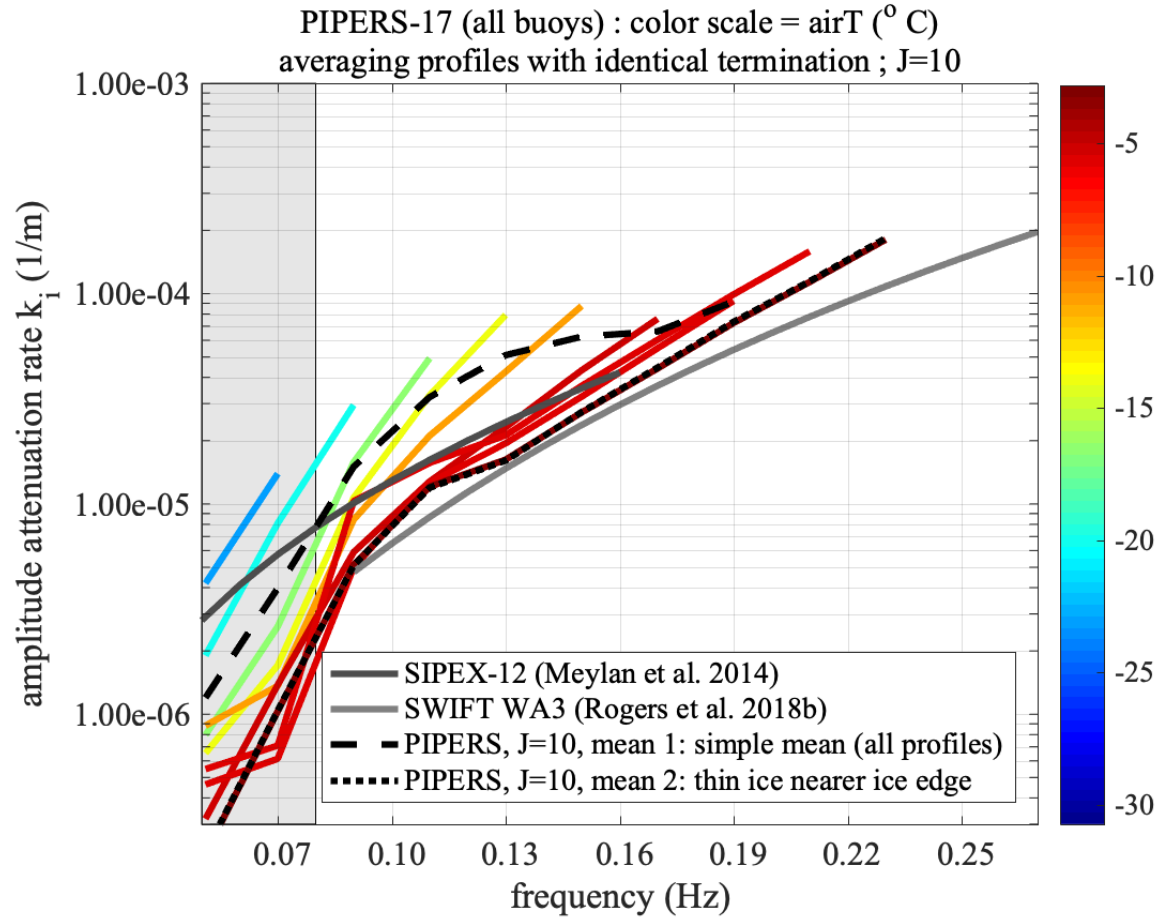
Figure 10. Like Figure 6 of the main text, except showing T_{air}.